Tropical Dynamics and Warming in Simplified Atmosphere–Ocean Simulations

P. J. TUCKMAN[a] AND JOHN MARSHALL[a]

[a] *Department of Earth, Atmospheric, and Planetary Sciences, Massachusetts Institute of Technology, Cambridge, Massachusetts*

(Manuscript received 5 December 2024, in final form 4 October 2025, accepted 1 November 2025)

ABSTRACT: The Hadley circulation, tropical sea surface temperatures (SSTs), and the tropical rain belt are key features of the tropical climate. In this work, we use simplified atmosphere–ocean simulations with no continents to study these phenomena and their response to greenhouse warming in an idealized setting. Without ocean dynamics, tropical precipitation strengthens with warming, while the Hadley circulation weakens but transports more energy out of the tropics. Meanwhile, the intertropical convergence zone (ITCZ) moves sinusoidally north and south following solar insolation over the seasonal cycle, and the meridional extent of this annual oscillation decreases with warming. In simulations with ocean dynamics, the ocean exports energy from the deep tropics, smoothing tropical SST gradients and creating an SST minimum at the equator. This leads to an ITCZ which straddles the equator in the annual mean and has a square-wave-like seasonal cycle, with rapid fall and spring transitions of peak precipitation between the hemispheres. Atmosphere and ocean changes with warming, as well as associated shifts in SST structure, are examined using an analytic framework based on a tropical energy balance model constructed from simple relationships between SST, mass transport, and energy transport. The simplified simulations and analytic model used here have implications for important features of the tropical climate such as the double-ITCZ bias, monsoon onset, and changes to the Hadley cells under greenhouse warming.

SIGNIFICANCE STATEMENT: Predicting how the tropical climate will change as the Earth warms is a societally important challenge. However, relevant phenomena such as the Hadley cells, the tropical rain belt, and ocean energy transport are complex and difficult to understand. Here, we systematically study how the tropics change under warming using simplified coupled atmosphere–ocean simulations and an energy budget model. We find that in warmer climates, the tropical rainband becomes stronger, Hadley cells weaken, tropical surface temperature gradients weaken, and the seasonal cycle of the tropical rainband shrinks.

KEYWORDS: Atmosphere-ocean interaction; Atmospheric circulation; Hadley circulation; Ocean circulation; Climate change; Surface temperature

1. Introduction

The intertropical convergence zone (ITCZ) is associated with intense precipitation encircling the Earth near the equator. The position of the ITCZ, its zonal structure, and its seasonal cycle are difficult to understand and predict (Schneider et al. 2014), so it can be useful to simulate the ITCZ in simplified systems and slowly increase the complexity (e.g., Blackburn and Hoskins 2013; Blackburn et al. 2013; Donohoe et al. 2014b; Geen et al. 2019; Wu et al. 2021). To this end, we study tropical SSTs, the ITCZ, and its seasonal cycle in aquaplanet simulations with and without a dynamic ocean, as well as the response of these systems to warming.

One of the simplest Earth-like systems used to study tropical dynamics is an atmospheric model coupled to a slab ocean (i.e., a fixed heat capacity surface that does not transport heat). Such simulations have been used to study the ITCZ in a variety of contexts, such as ITCZ shifts in response to imposed hemispheric asymmetries (Broccoli et al. 2006; Frierson and Hwang 2012; Kang et al. 2018) and the effect of the mixed-layer depth on the seasonal cycle (Donohoe et al. 2014b; Wang et al. 2019).

A step toward a more realistic Earth system can be taken either by parameterizing ocean heat transport in slab ocean simulations or by coupling the atmospheric model to a full ocean simulation. Ocean dynamics have been shown to have a significant effect on the ITCZ, such as by shifting the zonal and annual mean ITCZ to the north (Frierson et al. 2013; Marshall et al. 2014; Moreno-Chamarro et al. 2020) through the northward ocean heat transport of the Atlantic meridional overturning circulation (Buckley and Marshall 2016). Furthermore, tropical ocean circulations (often parameterized as Ekman heat transport; Codron 2012) dampen ITCZ shifts through a coupling of atmospheric Hadley cells with the subtropical ocean cells (Green and Marshall 2017; Kang et al. 2018; Green et al. 2019; Afargan-Gerstman and Adam 2020; Adam et al. 2023) and can push the ITCZ off the equator due to the cooling effect of equatorial upwelling (Bischoff and Schneider 2016; Adam 2021, 2023). Ocean dynamics have also been shown to weaken and widen the Hadley circulation by flattening SST gradients (Clement 2006; Hilgenbrink and Hartmann 2018).

There has been considerably less work on the seasonal cycle of the ITCZ in the presence of full ocean dynamics. However, some observations and simplified models indicate that

Supplemental information related to this paper is available at the Journals Online website: https://doi.org/10.1175/JCLI-D-24-0685.s1.

Corresponding author: P. J. Tuckman, ptuckman@mit.edu

DOI: 10.1175/JCLI-D-24-0685.1

when the ocean is active, there is a double ITCZ with a "seesaw response" over the seasonal cycle, in which the summer hemisphere ITCZ is stronger and the winter ITCZ is weaker (Zhao and Fedorov 2020; Adam et al. 2023).

The response of the ITCZ to greenhouse gas–induced warming has also received much attention in recent years (Frierson and Hwang 2012; Feldl and Bordoni 2016; Byrne et al. 2018), but mostly without considering the effect of ocean dynamics. In general, ITCZ precipitation is expected to intensify (Chou and Neelin 2004) with warming due to increases in low-level humidity. Meanwhile, the Hadley cells are expected to weaken and expand with warming (Levine and Schneider 2011; Lionello et al. 2024), while atmospheric poleward heat transport strengthens (Sobel and Camargo 2011; Huang et al. 2017; Ma et al. 2018), possibly as a result of increased static stability (Chemke and Polvani 2021).

Some research has been conducted on how ocean dynamics affect tropical climate under warming (Levine and Schneider 2011; Chemke 2021). It has been shown that 1) the weakening of the Atlantic meridional overturning circulation (AMOC) with warming will shift the ITCZ southward (Zhang and Delworth 2005), 2) the pattern of ocean warming causes an increase in ascent at the equator (Huang et al. 2017), and 3) ocean circulation weakens the response of the Hadley cell to warming by reducing the increase in SST (Chemke and Polvani 2018). Studies exploring the role of ocean dynamics have often used parameterized ocean heat transport or full GCMs, yet a conceptual framework for understanding how a dynamic ocean interacts with tropical circulations and warming does not currently exist.

Here, we take a systematic approach to understanding how Earth's tropics and the ITCZ change in response to warming with and without a dynamic ocean. We begin by studying an atmospheric model coupled to a slab ocean on an aquaplanet (labeled "slab") and study how tropical climate and the seasonal cycle respond to warming. We find that in these simulations, there is a strong, single, near-equator ITCZ which smoothly migrates north and south with the seasons. In warmer simulations, the Hadley circulation, and therefore the ascent in the ITCZ, is weaker, but precipitation is stronger due to large increases in surface specific humidity. In addition, the meridional extent of the seasonal cycle decreases with warming, associated with an increase in atmospheric heat capacity. When adding a dynamic ocean without any boundaries, ocean heat transport leads to an equatorial minimum of SST and, therefore, two off-equatorial ITCZs of which the summer hemisphere ITCZ is stronger. Ocean heat transport also adds to the poleward energy transport by the atmosphere, causing very flat SSTs in the deep tropics. The precipitation and SST minima on the equator weaken with warming, while the poleward ocean heat transport strengthens. We introduce a simple analytic energy balance model that explains these results by relating mass transport, energy transport, and SST gradients with or without ocean dynamics. We develop this analytic model in reference to the slab and dynamic ocean simulations and then apply it to a set of simulations with a single barrier to ocean flow.

Our paper is organized as follows. In section 2, we discuss the simulations used to study the tropical climate. In section 3, we analyze each set of simulations and introduce an energy balance model to understand how tropical SSTs and the Hadley circulation change with warming. Finally, section 4 summarizes our study and discusses its implications for more realistic systems and observations.

2. Simulations studied

The simulations used in this work are run using the MITgcm (Marshall et al. 1997; Tuckman et al. 2025) in coupled atmosphere–ocean configurations with no continents. Slab ocean simulations are run for 150 years, while dynamic ocean simulations are run for 750 years; data shown are averaged over the last 100 years of each simulation. The grid used is a cubed sphere with approximately 2.8° resolution for both the atmosphere and the ocean (Adcroft et al. 2004). The atmosphere has 26 vertical levels, idealized moist physics, a gray radiation scheme (Frierson et al. 2007), and water vapor feedback on longwave optical thickness (Byrne and O'Gorman 2013). There are no clouds and no shortwave absorption or reflection in the atmosphere. The albedo is thus equal to the prescribed surface albedo and is symmetric about the equator. The model has a seasonal cycle of insolation appropriate for a circular orbit with an obliquity of 23.45°. We run seven simulations in which the longwave absorption coefficient of CO_2 is varied in the gray radiation scheme, resulting in an ~3 K increase in tropical mean temperature between each simulation (Tuckman 2025). These experiments are labeled from 1 to 7, with the temperature increasing from 1 to 7; index 4 has the most Earth-like tropical temperatures (average SST from 20°S to 20°N is 27°C in the slab simulation).

The slab ocean configuration has a mixed-layer depth of 18 m, but simulations were run with 12 and 24 m without change to the qualitative results (see Donohoe et al. 2014b, for a discussion of the effect of mixed-layer depth). In our dynamic ocean simulations, the ocean has 15 vertical levels with a uniform depth of 3.4 km and no continental boundaries.

Figure 1 shows an overview of precipitation, SST, and tropical circulations from the simulations with Earth-like tropical temperatures (warming index 4). The slab ocean simulation is zonally symmetric, has maximum SST and precipitation on the equator, and has Hadley cells consisting of ascent on the equator and descent in the subtropics. The dynamic ocean simulation has two maxima of precipitation and SST, both slightly off the equator. Furthermore, the ascending branches of the Hadley cells are slightly off the equator in the lower troposphere, and there is an anti-Hadley circulation in the deep tropics. There are also oceanic subtropical cells extending deep into the ocean interior with upwelling on the equator.

3. Simulated tropical dynamics under warming

a. Slab ocean simulations

In this section, we discuss tropical climate, the ITCZ, and their response to warming in slab ocean simulations. Figure 2

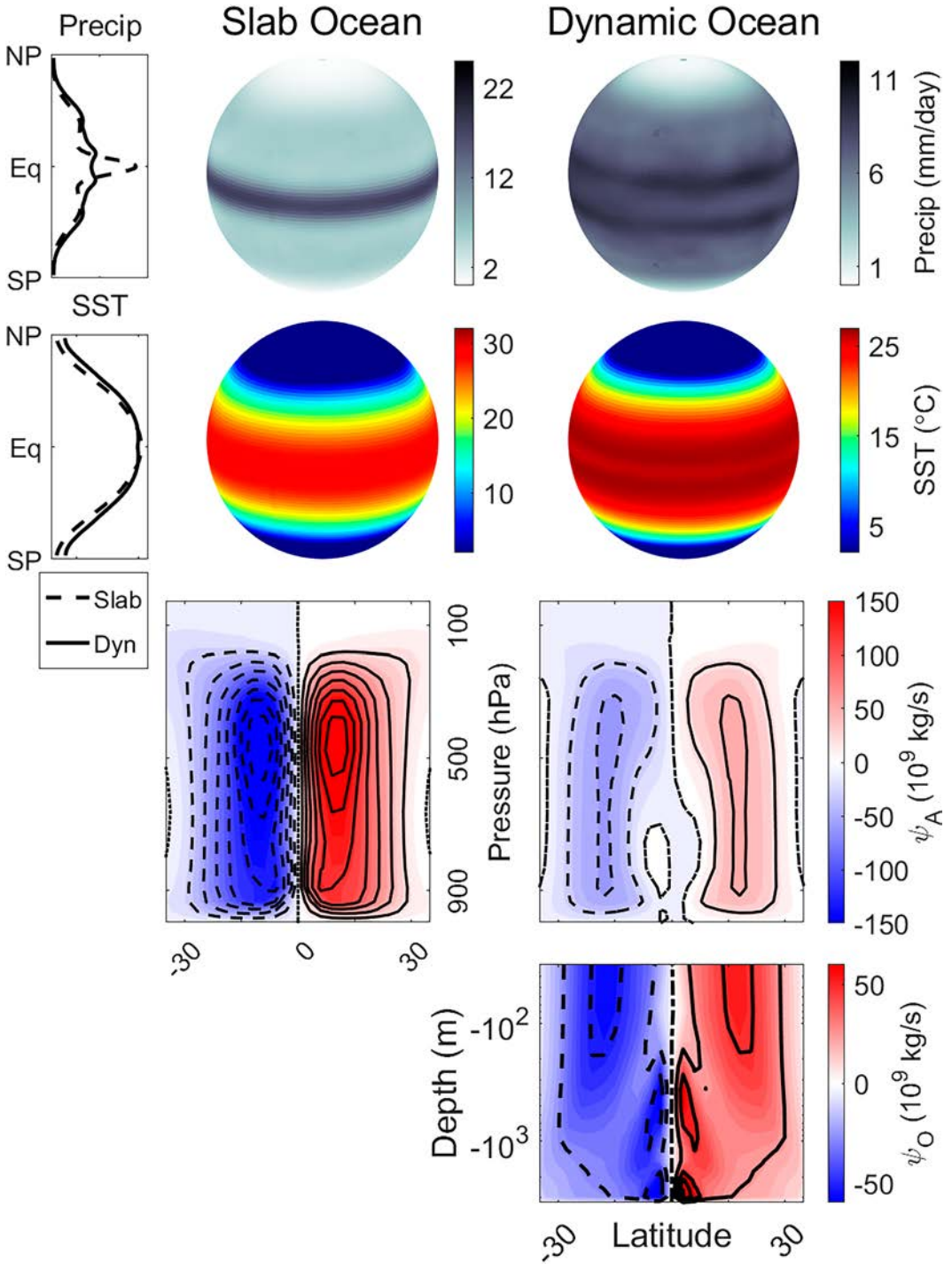

FIG. 1. Summary of our reference simulations (warming index 4), corresponding to present-day Earth-like tropical temperatures. The leftmost panels show the zonal-mean precipitation and SST from the slab (dashed) and dynamic ocean (solid) configurations; the left globes show quantities from the slab ocean configuration, and the right globes show quantities from the coupled atmosphere–ocean configuration. (top) Annual mean precipitation, (second row) annual mean SST, (third row) the atmospheric mass transport overturning streamfunction (positive indicates clockwise flow), and (bottom) the overturning streamfunction in the ocean. Contour lines in the streamfunction plots are placed at intervals of 25×10^9 kg s^{-1}, with solid lines indicating positive values and dashed lines indicating negative values.

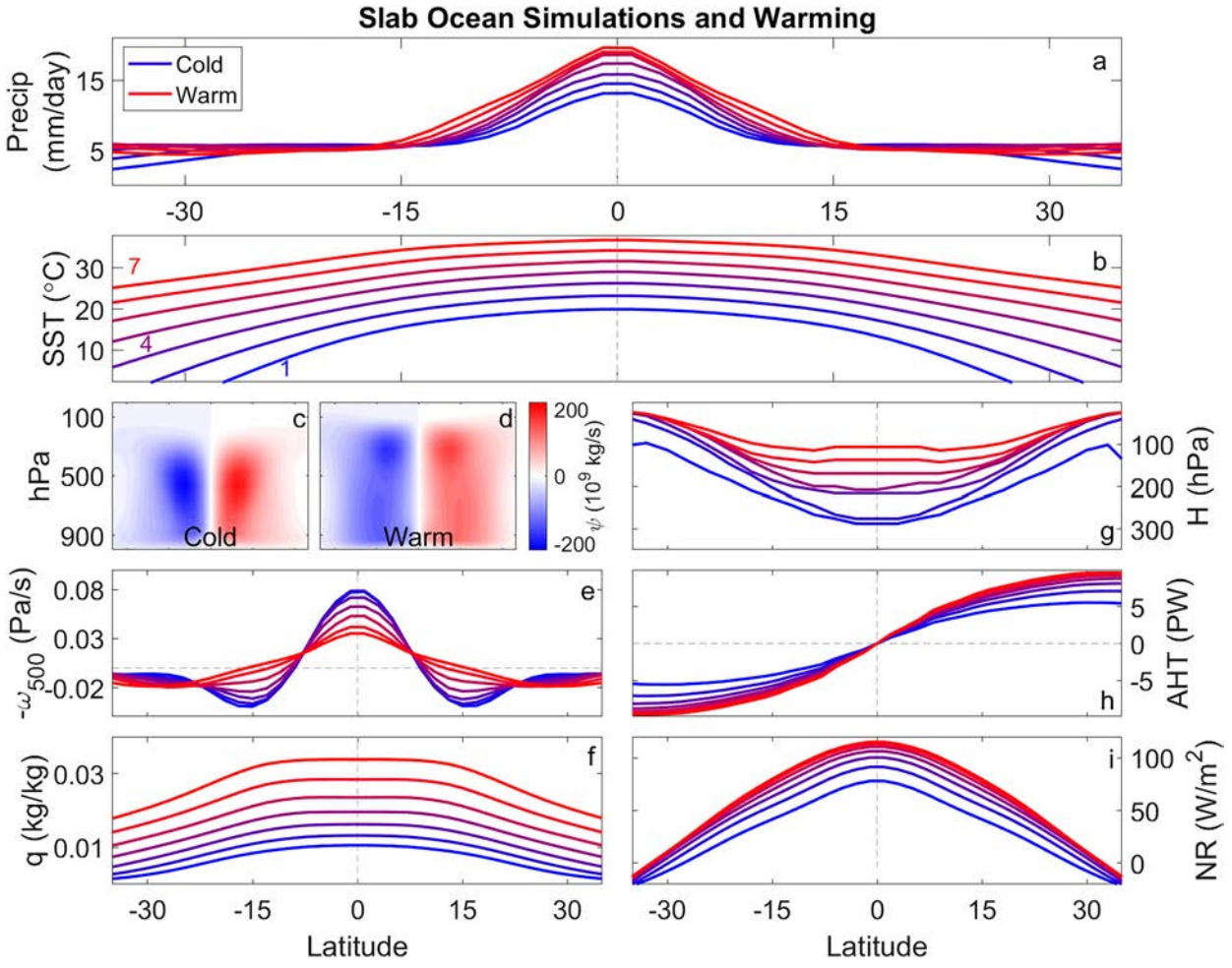

FIG. 2. The effect of warming (blue coldest, red warmest) in the slab ocean simulations on (a) precipitation, (b) SST, (c),(d) Hadley circulation streamfunctions from cold (index 2) and warm (index 6) simulations, (e) vertical velocity at ~500 hPa, (f) near-surface specific humidity, (g) tropopause height, (h) atmospheric heat transport, and (i) net TOA radiation, with positive indicating energy entering the atmosphere.

shows how several annual mean quantities change as more longwave radiation is absorbed in the atmosphere and the simulations become warmer (blue lines to red lines). In all simulations, annual mean precipitation has a single peak on the equator (Fig. 2a), and this peak increases in amplitude as temperature increases. SSTs (Fig. 2b) also have a single peak on the equator, and as the simulations warm, this peak flattens, with the drop in SST between the equator and 15°N being largest in the cold simulations and smaller in the warmer simulations (Burls and Fedorov 2014, 2017).

The Hadley cells, two examples of which are shown in Fig. 2c (simulation index 2) and (Fig. 2d) (index 6), become weaker, taller, and slightly wider in warmer simulations. The weakening of the circulation can also be seen in the 500-hPa vertical velocity (Fig. 2e). There is always ascent at the equator and descent in the subtropics, but the amplitude of vertical velocities is much greater for the cold simulations than for the warm simulations. Despite the weaker ascending motion, precipitation increases under warming (Fig. 2a); this can be explained by looking at low-level humidity (Fig. 2f). The increase in humidity and, therefore, condensable water vapor is a larger effect than the weakening of ascent, leading to an overall increase in precipitation (Held and Soden 2006). This humidity also leads to more condensation during deep convection and taller Hadley cells (cf. Fig. 2c and Fig. 2d), increasing the tropopause height (Fig. 2g), calculated as the height at which the Hadley streamfunction drops below 10% of its maximum value at that latitude (Santer et al. 2003a,b; Levine and Schneider 2011). The taller Hadley cells have a larger energy difference between their equatorward surface flow and poleward high-altitude flow, which we represent with the gross moist stability (GMS), defined as the difference in average tropical energy between the surface and the tropopause. The increase in GMS means that the Hadley cells export more energy from the deep tropics (Fig. 2h), despite a weakening of the overturning circulation. Finally, this change in horizontal atmospheric heat transport must be

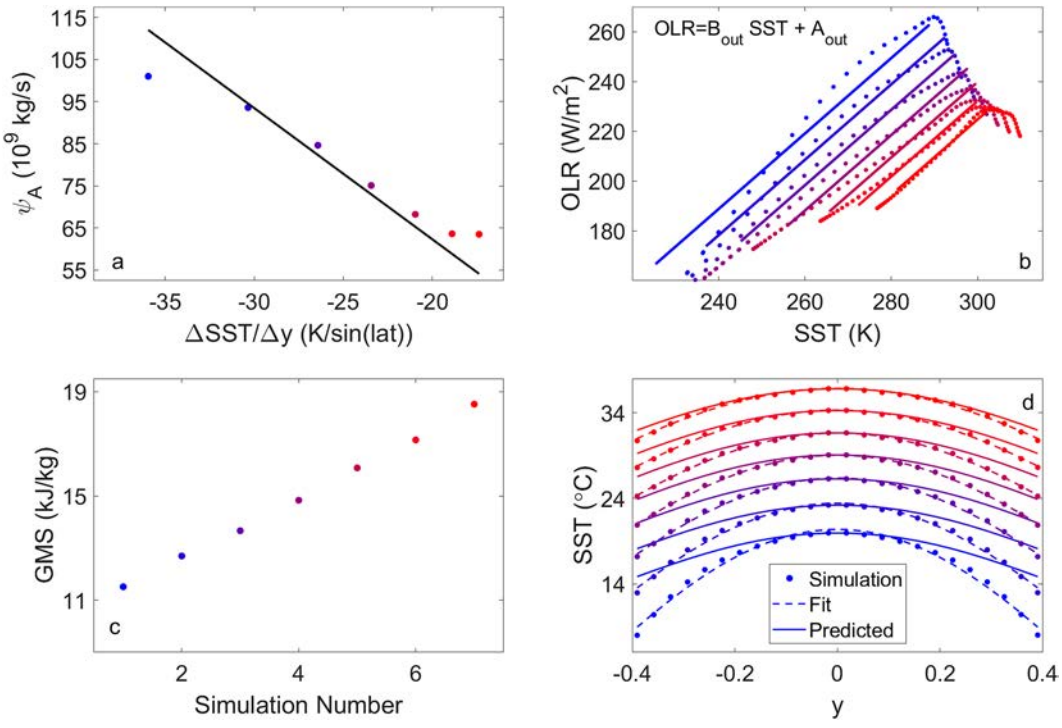

FIG. 3. Energy balance model assumptions and predictions compared to simulations: (a) the relationship between SST decrease from the equator to 25°N and mass transport along with a linear fit; (b) the relationship between SST and OLR; (c) the increase in GMS as the models become warmer (see Table 1); and (d) the simulated (dots), predicted (solid lines), and best fit (dashed lines) SST for each simulation (blue is coldest, red is warmest). Here, y is the sine of latitude.

balanced by a change in net top of atmosphere radiation to close the energy budget, as shown in Fig. 2i.

1) ENERGY BALANCE MODEL

Figure 2 shows that many aspects of tropical climate change with warming, and it can be difficult to disentangle cause and effect. Therefore, we formulate a simple energy balance model to help us understand the response of the system to warming. The variables of interest are vertically integrated atmospheric heat transport (AHT), the atmospheric mass streamfunction (ψ_A), the SST, and the top of atmosphere outgoing longwave radiation (OLR). Each of these quantities is a function of $y \equiv$ sin(latitude), and steady state is assumed. The complete system is as follows:

$$\psi_A = -\alpha \frac{d}{dy}\mathrm{SST}, \tag{1a}$$

$$\mathrm{OLR} = B_{\mathrm{out}}\mathrm{SST} + A_{\mathrm{out}}, \tag{1b}$$

$$\mathrm{AHT} = \mathrm{GMS}\psi_A, \tag{1c}$$

$$\frac{d}{dy}\mathrm{AHT} + \mathrm{OLR} = \mathrm{NSR}, \tag{1d}$$

where the net top of atmosphere solar radiation is NSR(y) and GMS is the gross moist stability of the Hadley circulation. We now discuss each equation in turn.

Equation (1a) relates the mass transport ψ_A to the SST gradient through a positive constant α. As SST peaks at the equator, the streamfunction will be negative in the Southern Hemisphere and positive in the Northern Hemisphere. In Fig. 3a, we plot the decrease in SST from the equator to 25°N against the magnitude of the streamfunction (i.e., ψ_A), taken to be half of its maximum value as a proxy for its average in the region. We see that mass transport is roughly linear in the SST difference, confirming that α can be treated as a constant across our simulations. Note that the physical mechanism behind this relationship is complex, as the strength of the Hadley circulation depends on several factors. Recent literature has indicated that ψ_A is at least partly driven by eddy momentum fluxes from the extratropics (Walker and Schneider 2006; Levine and Schneider 2011), which in turn depend on several quantities, including atmospheric available potential energy. This mechanism is discussed in appendix A, where it is shown that our simulations are consistent with this theory. Here, we assume that Hadley circulation strength is linear in the local SST gradients (which is consistent with the GCM results) to allow for an analytically solvable system. It should be noted that this qualitative connection between temperature gradients and Hadley circulation strength appears to hold in more realistic models (at least in the Northern Hemisphere; D'Agostino et al. 2017) and is consistent with the dual predictions of 1) polar amplified warming (Rantanen et al. 2022;

England and Feldl 2024) and 2) weakening of the Hadley circulation with warming (Hu et al. 2018; Lionello et al. 2024).

Equation (1b) states that the amount of longwave radiation that escapes to space is proportional to the SST with a constant offset, as is commonly assumed in energy balance models (Rose and Marshall 2009; Koll and Cronin 2018). The constant offset A_{out} changes across our simulations due to greenhouse warming and can be diagnosed from them, while B_{out} is taken to be the same across climates. The relationship is tested in Fig. 3b, where a fit is performed poleward of the latitude of the maximum OLR. The slope of the lines gives B_{out}, and the intercept gives A_{out}. The resulting fit is not good in the deep tropics (data points with high SST and negative slope) or in the coldest areas, but it is acceptable in the tropics. The reason for the large discrepancies in some areas is differences in humidity: An improved linear model for OLR based on SST and total column water can be constructed (not shown) but would require a prediction of the humidity field and so is not employed here.

Equation (1c) assumes that AHT is the product of ψ_A and GMS, where GMS is calculated as the difference in moist static energy (MSE) between the tropopause and the surface. Note that this assumption fails when the eddy transport is significant or there are shallow and deep circulations at the same latitude (Neelin and Held 1987). The GMS can be defined in various ways (e.g., Raymond et al. 2009; Yu et al. 1998; Inoue and Back 2017); the simple form chosen in Eq. (1c) has been used previously (Held 2001; Czaja and Marshall 2006) and is the most intuitive. In Fig. 2, it was shown that the tropopause height increases with warming; this leads to an ~80% increase in GMS between the coldest and warmest simulations, mainly due to an increase in the geopotential height of the tropopause (Fig. 3c, when calculating GMS, the tropopause is defined as the largest pressure where $|\psi| < 20 \times 10^9$ kg s^{-1}). Here, we assume that GMS is constant with latitude throughout the Hadley cells, which is not precisely true. Allowing GMS to vary as a function of y can be included in the model and does not significantly change the predicted SST; this is discussed in appendix B. Additionally, it is important to note that the vertical structure of the Hadley cells may change with warming, implying that the simplified GMS parameter used here may not capture the full relationship between energy transport and mass transport.

Equation (1d) simply states that there is a balance between energy transport, longwave radiation, and net solar radiation, ensuring that energy is conserved.

The complete system comprises four equations with four unknowns and can therefore be transformed into a single equation for SST using Eqs. (1a) and (1c) to replace AHT in the last equation and Eq. (1b) to replace OLR. This gives

$$-C_A \kappa_A \frac{d^2}{dy^2}\text{SST} + B_{\text{out}}\text{SST} = \text{NSR} - A_{\text{out}}, \tag{2}$$

where

$$\kappa_A \equiv \alpha \text{GMS}/C_A \tag{3}$$

is an atmospheric horizontal diffusion coefficient and C_A is the effective heat capacity of the atmospheric column, or the change in energy of the column corresponding to a 1° change of SST.

Equation (2) summarizes atmospheric heat transport in terms of a single mixing coefficient κ_A. Atmospheric heat transport mixing SST gradients is a common assumption in tropical dynamics (Craig and Mack 2013; Hottovy and Stechmann 2015; Ahmed and Neelin 2019; Siler et al. 2018); previous work (e.g., Hwang and Frierson 2010) often assumes that κ_A is constant, but here we allow it to change as the atmosphere warms.

Relevant solutions to Eq. (2) can be found by prescribing the forcing as NSR $\equiv S_0 \cos(y/L_s)$, where S_O is the solar constant and L_s is a solar radiation length scale, then setting $d\text{SST}/dy = 0$ at the equator:

$$\text{SST} = \text{SST}_0 \cosh(y/\lambda) + \frac{S_0}{B_{\text{out}}}\frac{\cos(y/L_s)}{1 + \lambda^2/L_s^2} - \frac{A_{\text{out}}}{B_{\text{out}}}, \tag{4}$$

where the dynamical length scale λ is given by

$$\lambda \equiv \sqrt{C_A \kappa_A / B_{\text{out}}} = \sqrt{\alpha \text{GMS}/B_{\text{out}}}, \tag{5}$$

and SST_0 is a constant which can be determined by fitting our solutions to the value of SST at the equator. The parameter λ appears in energy balance models (see, e.g., Rose and Marshall 2009) as the scale over which dynamics (represented by κ_A) smooth out temperature gradients on a radiative time scale (C_A/B_{out}).

The three terms of Eq. (4) represent the factors that control SST. The third term, $A_{\text{out}}/B_{\text{out}}$, does not depend on latitude and represents the uniform warming caused by increasing the longwave optical thickness of the atmosphere (i.e., the greenhouse effect decreases A_{out} and uniformly warms the surface). The second term is directly forced by sunlight, causing warmer SSTs at the equator and cooler SSTs when $|y|$ grows. This term is slightly modulated by dynamics through λ in the denominator, but this effect does not depend on latitude. The first term, meanwhile, controls how the SST gradient changes with warming, as λ, which depends on GMS, sets the length scale of the hyperbolic cosine. This term increases with y, as atmospheric heat transport moves energy away from the equator and toward the poles, i.e., atmospheric dynamics cool the equator and warm the extratropics. Figure 2 showed that the Hadley cells become deeper with warming, indicating an increase in GMS. According to Eqs. (4) and (5), this increase in GMS will decrease the relative importance of sunlight (due to λ being in the denominator of the second term), making atmospheric heat transport more important. As the AHT term increases away from the equator, the resulting SST curve will be flatter.

We can test our analytic model in two ways: 1) by fitting our expression, Eq. (4), to the simulated SST profiles by adjusting λ and SST_0 and 2) by predicting λ from Eq. (3) based on the diagnostics of α, GMS, and B_{out}. The results of both

TABLE 1. Key quantities and predictions from the energy balance model diagnosed from the seven atmospheric warming experiments coupled to a slab ocean. Quantities are calculated as described in the main text (averaged within 25° of the equator), while C_A is calculated as the slope of the line of best fit between the zonal mean tropical column integrated atmospheric energy and SST. The variables A_{out} and GMS are defined in Eqs. (1b) and (1c), κ_A and C_A are defined in Eqs. (2) and (3), while SST_0 and λ are defined in Eqs. (4) and (5).

Simulation number	A_{out} (W m^{-2})	GMS (kJ kg^{-1})	$\kappa_A C_A$ (10^{13} W K^{-1})	C_A (10^6 J m^{-2} K)	κ_A (10^6 m^2 s^{-1})	Predicted λ	Predicted SST_0	Fitted λ	Fitted SST_0
1	−175	11.5	3.59	8.20	4.37	0.74	82.7	0.50	40.5
2	−186	12.7	3.96	10.5	3.76	0.78	84.2	0.56	49.1
3	−196	13.7	4.26	13.3	3.21	0.81	84.4	0.62	55.9
4	−206	14.8	4.62	16.5	2.79	0.84	84.7	0.68	61.9
5	−215	16.1	5.01	20.7	2.42	0.87	85.4	0.74	67.4
6	−223	17.1	5.34	25.9	2.06	0.90	86.2	0.79	72.9
7	−230	18.5	5.77	31.6	1.82	0.94	87.6	0.85	78.3

are shown in Fig. 3d. We see that the fitted model matches SSTs almost exactly, and the predicted model does reasonably well but is not perfect. Specifically, the predicted model correctly shows an increase in λ with warming, but the predicted λ is generally too large, and changes across the simulations are somewhat too small, resulting in λ that is significantly too high for the cold simulations. Allowing GMS to vary with latitude makes the SST predictions for the coldest simulations slightly more accurate but does not allow analytical solutions (appendix B). The relevant constants are calculated as $B_{out} = 1.5$ W m^{-2} K^{-1}, $\alpha = 3.1 \times 10^9$ kg S^{-1} K^{-1}, $L_s = 0.65$, and $S_0 = 333.2$ W m^{-2}; A_{out}, GMS, κ_A, C_A, the length scales, and the SST_0 values are shown in Table 1.

The quantities in Table 1 allow us to interpret the change in SST with warming through changes in αGMS or $\kappa_A C_A$ [these are equal to each other, Eq. (3)]. As discussed above, GMS increases with warming while α remains constant, leading to an increase in the length scale. Physically, the temperature gradient decreases, slowing the Hadley circulation. However, the Hadley cells transport more energy due to the increasing energy difference across them (i.e., increasing GMS; Hwang and Frierson 2010). Importantly, as α is constant and $\lambda \sim \sqrt{\alpha \mathrm{GMS}}$, GMS alone controls the SST decrease away from the equator in this system. The implication is that even as the Hadley cell weakens with warming due to a flattening SST gradient, that effect cannot prevent the smoothing of SST by increased heat transport.

Another way to view the same phenomenon is that C_A increases very quickly with warming (Table 1, Cronin and Emanuel 2013), indicating that each parcel of air moving through the Hadley circulation transports more energy. However, the diffusivity decreases because of the slower overturning of mass in the Hadley cells.

In summary, warming a slab ocean system increases precipitation rates and atmospheric heat transport while weakening SST gradients and the Hadley circulation. The strengthening of heat transport, which leads to weaker SST gradients despite a weakening Hadley circulation, is a consequence of an increase in GMS, making the atmosphere more efficient at transporting energy away from the equator.

2) THE SEASONAL CYCLE

We now turn to the seasonal cycle of the ITCZ in the slab ocean simulations. Figures 4a and 4b show precipitation as a function of latitude and month for simulation warming indices 2 (Fig. 4a) and 6 (Fig. 4b). Both have strong, clearly defined single ITCZs that move smoothly north and south during the seasonal cycle. The main differences are that the warmer simulation has 1) more precipitation and 2) less movement of the ITCZ, reaching only 3°N, while the colder simulation reaches 4.7°N. This trend of warmer simulations having a smaller seasonal cycle is generally true (Fig. 4c) but is a large effect only for the warmer simulations. The four coldest simulations have ITCZ seasonalities of around 4.5°–5°, while the warmer ones have smaller amplitudes (Fig. 4d). This shrinking of the seasonality of the ITCZ position follows the seasonality of the near-surface MSE maximum (squares, Fig. 4d), consistent with convective quasi equilibrium (Emanuel et al. 1994; Emanuel 2019). In other words, if we can understand what sets the latitude of the MSE maximum, the extent of the seasonal migration of the ITCZ will follow.

Assuming that the annual mean MSE peak is on the equator, the seasonality of the MSE maximum will depend principally on the annual mean decrease in MSE away from the equator. If MSE is very flat in the annual mean, then it will be easy for the MSE maximum, and therefore the ITCZ, to reach far away from the equator in a solstitial season. However, if MSE is very sharply peaked, then the ITCZ will be stuck near the equator year-round. Note that this assumes that the energy input to the system does not change with warming, which is mostly true because solar insolation is constant across the simulations.

We show the annual mean MSE gradient in Fig. 4e. Interestingly, the MSE gradient steepens with warming, unlike the previously discussed SST gradient. These are not inconsistent because the heat capacity of a parcel of air, i.e., the change in MSE per degree temperature increase, rises rapidly with warming. Therefore, the same change in SST can imply a larger change in near-surface MSE (Fig. 4f) in warmer simulations. This is due to the exponential relationship between temperature and water content (at constant relative humidity, i.e., the Clausius–Clapeyron relation; Clapeyron 1834). In

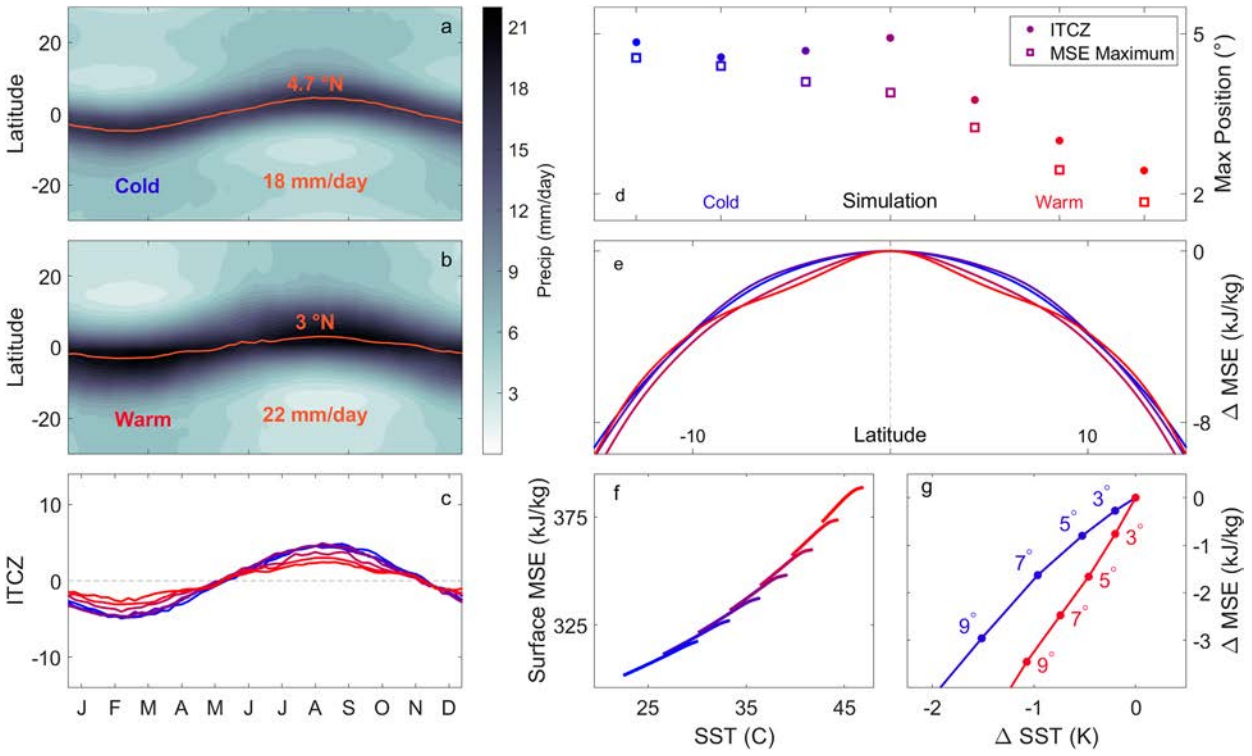

FIG. 4. The seasonal cycle of ITCZ position in the slab ocean simulations. (a),(b) Precipitation as a function of latitude and month in the second coldest and second warmest simulations, and the ITCZ position is highlighted with an orange line. The seasonal cycle of ITCZ position is shown for all slab ocean simulations in (c). (d) The maximum ITCZ position and the northernmost position of the near-surface (~975 hPa) MSE maximum. (e) The annual mean MSE decrease away from the equator. (f),(g) The relationship between MSE and SST, in absolute terms for all simulations [(f), within 20° of the equator] and as a difference from the equator in simulations 2 and 6 (g).

other words, a given change in SST corresponds to a larger change in humidity, and therefore MSE, in a warmer climate. This is shown explicitly for the second and sixth simulations in Fig. 4g. As we move away from the equator, both SST and MSE decrease (down and left). In the warmer simulation, SST decreases more slowly with latitude; e.g., at 9°N, the cold simulation SST changed by approximately 1.5°C, while the warm simulation SST has changed by only 1°C. However, as the heat capacity of the warm simulation is greater, this smaller change in SST corresponds to a larger change in surface MSE (-3.5 kJ kg^{-1} instead of -3). Therefore, the warmer simulations have steeper MSE gradients, keeping the ITCZ near the equator. In other words, the higher heat capacities of warmer systems make it harder to overcome the annual mean energy gradients, so the ITCZ seasonality shrinks with warming. Note that the MSE gradients being larger in warmer simulations are also consistent with the diffusion of energy in the system decreasing, as discussed in the previous section (i.e., κ_A decreasing).

In summary, a system with full atmospheric dynamics but no active ocean has a strong, single ITCZ that migrates smoothly over the seasonal cycle. When the system warms, the SST gradients flatten, the Hadley cells weaken, the ITCZ strengthens, and the amplitude of the seasonality of the ITCZ shrinks. Elements of these changes have been discussed previously (e.g., Gastineau et al. 2009; Ma et al. 2018; Judd et al. 2024); we have here explained how these changes fit together and can be viewed as being driven by thermodynamic changes.

b. *Dynamic ocean simulations*

In this section, we discuss simulations with a full dynamic ocean but no continental boundaries. We begin by comparing the annual mean climate of a dynamic ocean simulation to that of a slab ocean simulation at Earth-like temperatures (Fig. 5). The SST in the slab ocean simulation (dashed line, Fig. 5a) peaks at the equator and decreases toward the poles; these features do not depend strongly on slab ocean depth (not shown, verified in simulations with slab ocean depths up to 500 m). The dynamic ocean SST (solid line), on the other hand, is much flatter in the deep tropics (within ±15°) and has a minimum at the equator. This has a dramatic effect on the annual mean precipitation (Fig. 5b): slab ocean simulation has a large single-peak ITCZ corresponding to its SST maximum on the equator, but the dynamic simulation has two much smaller peaks about 7° off the equator in each direction. This precipitation difference is a manifestation of changes in the Hadley circulation, shown in Fig. 5c. In the slab ocean case (Fig. 1), there is ascent throughout the troposphere above the equator, and the streamfunction has a magnitude of ~150 × 10^9 kg s^{-1}. In the dynamic ocean simulation (Fig. 5c), on the other hand,

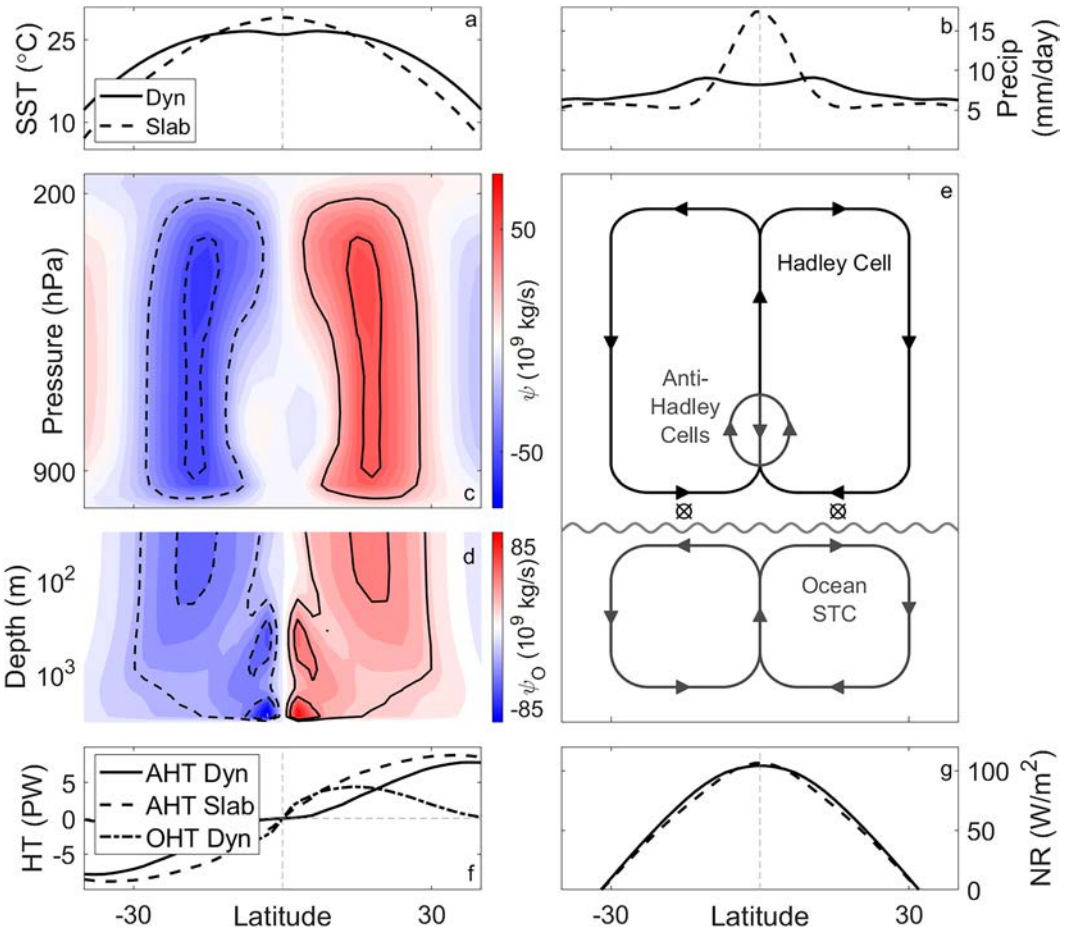

FIG. 5. A comparison of the slab (dashed) and dynamic ocean (solid) simulations (warming index 4, i.e., Earth-like temperatures). The following quantities are plotted as a function of latitude in the tropics: zonal and annual mean (a) SST, (b) precipitation, (c) Hadley cell streamfunctions, (d) ocean subtropical cell streamfunctions, (e) a schematic of the tropical circulations, (f) heat transport in the atmosphere and ocean, and (g) net TOA radiation. In the schematic, circles with a cross indicate winds into the page, while curved rectangles represent circulations in the directions indicated.

the magnitude of the streamfunction is of order $\sim 75 \times 10^9\,\mathrm{kg\,s^{-1}}$, and there is a small anti-Hadley circulation in the lower troposphere at the equator. This anti-Hadley circulation, driven by the SST minimum at the equator, has previously been discussed with respect to idealized simulations (Bischoff and Schneider 2016; Adam 2021, 2023) and theories of tropical energy transport (Bischoff and Schneider 2016; Adam et al. 2016; Adam 2023) and can be observed in the region of the cold tongue of the east Pacific (especially in Southern Hemisphere summer and fall; Adam et al. 2018).

The root cause of this SST structure is the subtropical cells of the ocean (streamfunctions in Fig. 5d). The equatorward surface winds associated with the Hadley cells lead to trade winds, or surface tropical easterlies, shown in a schematic in Fig. 5e. These easterlies drive ocean flow in the Ekman layer perpendicular to the direction of the wind, leading to poleward surface currents in the tropics. The water moved poleward by the surface current is replaced through upwelling, cooling the surface water at the equator and causing an SST minimum (Fig. 5a). These surface Ekman currents also carry energy poleward; the ocean (dashed–dotted line) and atmosphere (solid) heat transports are shown in Fig. 5f, where they are compared to the slab ocean heat transport (dashed). We see that in the deep tropics, the atmospheric energy transport is close to zero, and the ocean heat transport nearly exactly matches the atmosphere heat transport from the slab ocean case. In the subtropics, both atmospheric and ocean heat transports are important, and in the extratropics, atmospheric heat transport is dominant (Held 2001; Czaja and Marshall 2006). The excess total energy transport away from the equator in the dynamic ocean simulation is balanced by a change in the top of atmosphere net radiation, shown in Fig. 5g.

Overall, Ekman transport driven by the trade winds associated with the Hadley cells causes equatorial upwelling when a dynamic ocean is included in the simulation. This creates SST and precipitation minima at the equator, leading to a small

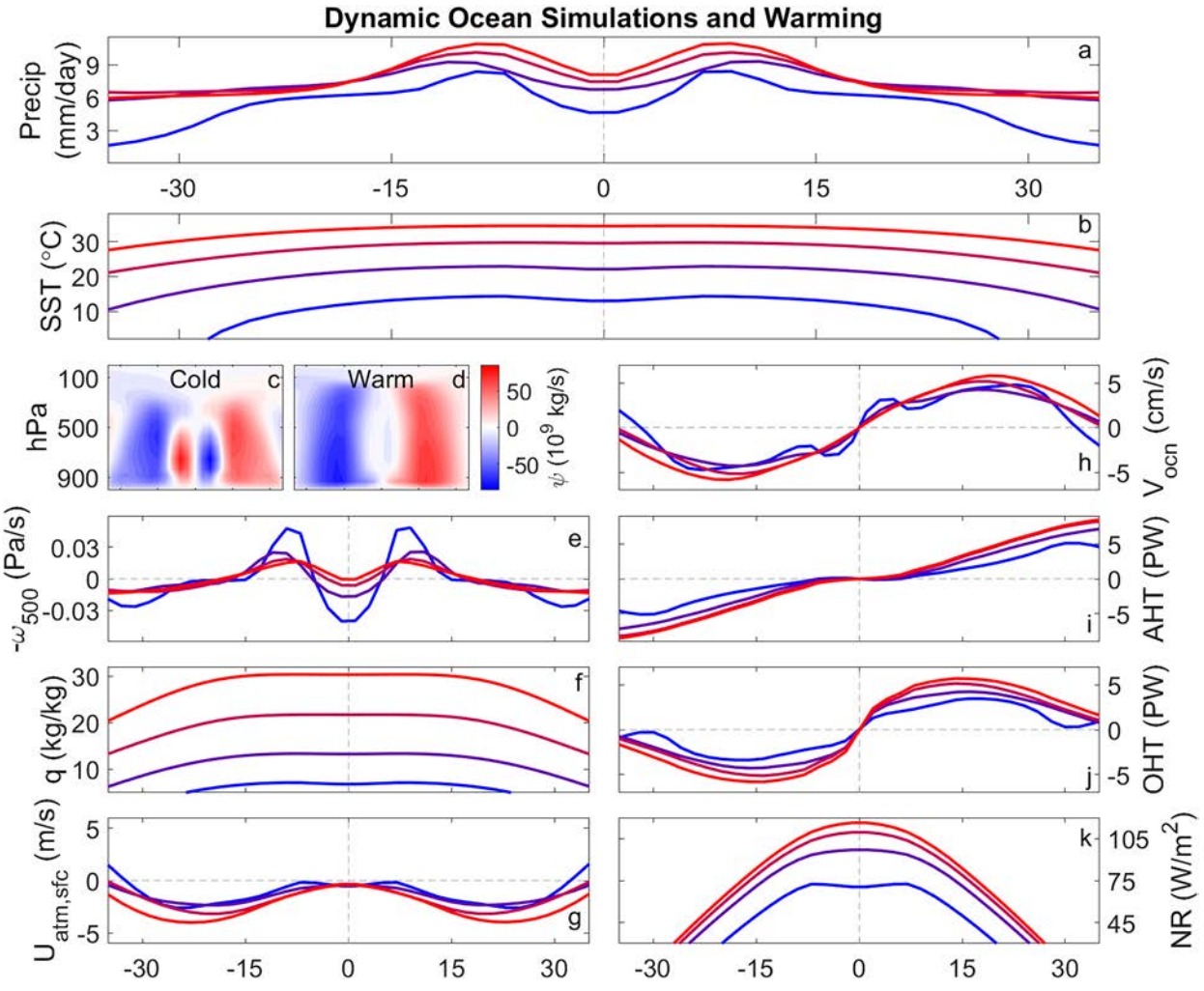

FIG. 6. As in Fig. 2, but for the dynamic ocean simulations, indices 1, 3, 5, and 7. The quantities shown are (a) precipitation, (b) SST, (c),(d) two sample Hadley cell streamfunctions, (e) vertical velocity at ~500 hPa, (f) near-surface specific humidity, (g) near-surface zonal wind, (h) near-surface meridional current, (i) atmospheric heat transport, (j) ocean heat transport, and (k) net radiation.

anti-Hadley circulation and a double ITCZ in the annual mean.

The impact of a dynamic ocean on atmospheric circulation changes as we warm (or cool) the system. Figure 6 shows how the relevant quantities change, starting with precipitation (Fig. 6a). As in the slab ocean case, precipitation increases with warming, but the overall structure remains the same, with two peaks a few degrees off the equator in each direction. The gradient of SST (Fig. 6b) once again flattens with warming, i.e., the difference between the maximum SST and extratropical SST decreases with warming. The equatorial SST minima also become shallower with warming as the atmosphere becomes more efficient at smoothing out SST gradients, until in the warmest cases it is almost nonexistent.

The SST changes with warming have the expected impacts on the Hadley cells, as colder simulations (Fig. 6c) have much stronger anti-Hadley cells than warmer simulations (Fig. 6d), and vertical velocity weakens with warming (Fig. 6e). As before, precipitation increases because the enhanced humidity (Fig. 6f) is enough to overcome the decrease in vertical velocity.

Despite a weakening of vertical velocities, the horizontal surface winds associated with the Hadley cells actually strengthen with warming (Fig. 6g). This is not inconsistent, as the width of the Hadley cells also increases. Zonal-mean mass conservation in the atmosphere can be written as $d\omega/dp = -dv/dy$, where v is the meridional surface wind. Although the amplitude of the left-hand side decreases with warming, dy increases because the anti-Hadley cells are shrinking. This allows v to increase despite the weakening of vertical mass transport. As the Coriolis effect remains the same, the zonal wind (Fig. 6g) also strengthens. These trade winds then drive ocean circulation, causing the poleward flow of the surface ocean to strengthen with warming (Fig. 6h).

As in the slab ocean simulation, atmospheric heat transport increases with warming (Fig. 6i) due to the heightening of the tropopause (cf. Fig. 6c and Fig. 6d). The ocean heat transport

also increases with warming (Fig. 6j) due to the increasing horizontal surface winds. This means that the overall equator-to-pole energy transport of the coupled system increases rather rapidly with warming. This is compensated by a change in net radiation (Fig. 6k) as top of atmosphere OLR decreases due to increasing longwave optical thickness.

1) ENERGY BALANCE MODEL WITH AN OCEAN

To apply our analytic model to dynamic ocean simulations, we must develop an expression for ocean heat transport (OHT). Similarly to atmospheric heat transport, OHT can be defined as the product of a gross moist stability (GMS_O) and an overturning streamfunction (ψ_O), where GMS_O is the difference in energy between the top and bottom of the circulation, assumed here to be at the surface and 1000 m, respectively. As the specific heat of water ($\approx$4000 J kg^{-1} K^{-1}) is roughly constant, GMS_O is proportional to the temperature difference between the surface and the bottom of the circulation. We therefore write

$$\mathrm{OHT} = \psi_O \mathrm{GMS}_O = \psi_O c_p (T_{\mathrm{sfc}} - T_{\mathrm{depth}}), \tag{6}$$

where c_p is the specific heat of seawater.

If we assume that the movement of water below the surface is adiabatic, then this vertical temperature difference is equivalent to a horizontal temperature difference across the circulation (Held 2001). This can be understood by tracking a parcel of water through a subtropical cell: Water rises at the equator, is heated by the sun but cooled by the atmosphere when on the surface, and then descends in the subtropics. During the return from the subtropics to the equator at depth, there are no major sources or sinks of energy, so the parcel's temperature remains constant. In other words, GMS_O depends on a meridional temperature difference because the water at the bottom of the subtropical cell has its properties set at the surface when it sinks. We can therefore write

$$\begin{aligned}\mathrm{OHT} &= \psi_O c_p (\mathrm{SST}_{\mathrm{max}} - \mathrm{SST}_{\mathrm{ET}}) \\ &= -\psi_O c_p \Delta y \frac{d\mathrm{SST}}{dy},\end{aligned} \tag{7}$$

where $\mathrm{SST}_{\mathrm{max}} - \mathrm{SST}_{\mathrm{ET}}$ is the difference in SST between its maximum and the extratropics and Δy is the distance between these SST values. For our purposes, the extratropical SST is measured at the latitude where the near-surface ocean streamfunction goes from positive to negative in the Northern Hemisphere. We can also replace the ocean streamfunction with its driver, the near-surface zonal wind. The subtropical cells are controlled by surface winds, so we will assume that $\psi_O = -\beta U_{\mathrm{atm}}$, where β is a positive constant and U_{atm} is the average near-surface zonal wind between the equator and 35°N (negative in the simulations studied). This assumption is supported by our simulations: ψ_O and U_{atm} are very strongly correlated (Fig. S1 in the online supplemental material). Note that one might assume that $\psi_O \approx \psi_A$ (Held 2001), but that relationship does not hold in the simulations studied here likely due to momentum transport by synoptic eddies being nonnegligible in the region studied.

Our final expression for ocean heat transport is therefore

$$\mathrm{OHT} = c_p \beta U_{\mathrm{atm}} \Delta y \frac{d\mathrm{SST}}{dy}, \tag{8}$$

where $\beta = 12.5 \times 10^9$ kg m^{-1} and $c_p = 4000$ J kg^{-1} K^{-1} are constants. This suggests that OHT can now be viewed as a diffusive process, i.e.,

$$\mathrm{OHT} = -\kappa_O C_O \frac{d\mathrm{SST}}{dy}, \tag{9}$$

where C_O is the heat capacity of 1000 m of water ($4\ \mathrm{J} \times 10^9$ J m^{-2} K^{-1}) and κ_O is an ocean diffusivity given by

$$\kappa_O \equiv -\beta U_{\mathrm{atm}} \frac{c_p}{C_O} \Delta y. \tag{10}$$

Note that the above does not imply that changes in OHT with warming can be predicted from only the meridional gradient of SST since κ_O is not a constant. Instead, the meridional extent of the subtropical cells and the near-surface wind speed change; in this model, these changes are included in κ_O.

Using this expression, we can incorporate OHT into the energy budget equation by replacing $\kappa_A C_A$ with $\kappa_A C_A + \kappa_O C_O$:

$$-(C_A \kappa_A + C_O \kappa_O) \frac{d^2}{dy^2} \mathrm{SST} + B_{\mathrm{out}} \mathrm{SST} = \mathrm{NSR} - A_{\mathrm{out}}, \tag{11}$$

which allows us to identify an ocean length scale $\lambda_O = \sqrt{\kappa_O C_O / B_{\mathrm{out}}}$ and a coupled length scale:

$$\lambda_c = \sqrt{\frac{\kappa_A C_A + \kappa_O C_O}{B_{\mathrm{out}}}}. \tag{12}$$

This formulation can also be used to calculate a coupled diffusivity such that $\kappa_C \times (C_A + C_O) = \kappa_A C_A + \kappa_O C_O$.

We compare these predicted atmosphere and ocean quantities to our simulations in Fig. 7. As in the case of the slab ocean, the atmospheric length scale (left panel, green line) increases with warming due to an increase in gross moist stability (since α and B_{out} are constants). If our analytic model was not modified to take into account ocean heat transport, this would be the prediction for SST length scale and would be far off from that found in the coupled simulations (dashed black line). The oceanic length scale (orange line) is similar to that of the atmosphere and also increases with warming. The combined growth of atmospheric and oceanic length scales causes the predicted coupled length scale (solid black line) to increase by almost a factor of 2 between the coldest and warmest simulations. This is in general agreement with the simulated SST length scale, as it also increases rapidly with warming. We can also test our idealized model by directly comparing predicted and simulated SSTs (right panel). Both the fit and the predicted SSTs match the simulations very well. However, they fail to capture the equatorial minimum

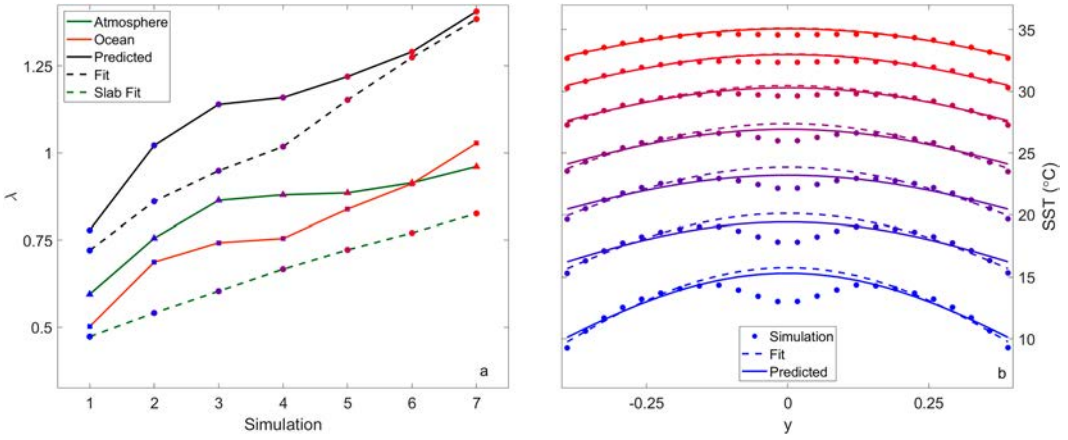

FIG. 7. Comparing the prediction from our energy balance model to dynamic ocean simulations. (left) The predicted atmosphere, ocean, and coupled length scales, as well as the fitted length scale to the aquaplanet simulation SSTs. (right) The simulated SST as a function of latitude (scatterplot), the predicted coupled SST (solid lines), and the best fit SSTs (dashed).

because our model does not include localized upwelling on the equator.

We can understand the changes in the length scale by looking at the relevant quantities for the coupled model (Table 2). As in the case of the slab ocean, atmospheric GMS and heat capacity increase rapidly with warming, while mass transport and diffusivity decrease slowly. The net result is that the atmospheric heat transport and length scale increase with warming. In the ocean, the heat capacity is assumed to be constant, but the strength of the overturning cell (ψ_O) and its width (Δy) both increase with warming, leading to a large increase in the predicted ocean diffusivity (κ_O). The strength of the overturning cell is, in turn, driven by U_{atm}, which is greater in warmer climates as the Hadley cell widens (cf. Figs. 6c,d). This increases the ocean length scale, leading to a very fast increase in the predicted coupled heat transport and length scale with warming. The model prediction is in approximate agreement with the simulations, in which we also see an increase in coupled diffusivity and the SST length scale.

In summary, ocean dynamics create a slight equatorial minimum of SST and smooth the tropical SST gradient by moving energy away from the equator (Fig. 8a). This heat transport, just as with atmospheric heat transport, can be represented as a diffusive process which strengthens with warming. As the system warms and diffuses temperature away from the equator more effectively, the equatorial minimum and tropical–extratropical temperature difference both weaken.

Figure 8 also shows how the total tropical heat transport changes with warming. In the coldest simulation, coupled atmosphere–ocean heat transport is roughly the same as the atmospheric heat transport from the slab ocean simulation. However, the total heat transport from the coupled simulation increases faster than that of the slab simulation (Fig. 8b) due to both atmosphere and ocean heat transport increasing with warming (Fig. 8c). These results show that if we wish to understand how tropical dynamics and energy transport change with warming, both atmospheric and oceanic effects must be considered.

2) THE SEASONAL CYCLE

The seasonal cycle of the ITCZ in a dynamic ocean simulation is very different from that of a slab ocean. Figure 9a shows the zonal mean precipitation as a function of latitude and month in the index 2 simulation. There are two peaks of precipitation throughout the year, one just north of the cold equatorial region and one just south. The ITCZ moves between these two precipitation peaks, jumping toward the spring hemisphere (Zhao and Fedorov 2020). This is also found in simulation index 6 (Fig. 9b), but with more precipitation (peaking at 16 mm day^{-1}) and with a slightly smaller maximum latitude of the ITCZ.

As the ITCZ is defined as the latitude of global maximum precipitation, and there are two local maxima of precipitation year round, the ITCZ will reside in whichever hemisphere has the larger precipitation peak. At the beginning of the year, there is a strong precipitation band in the Southern Hemisphere (Fig. 9c, dashed) and a weak one in the Northern Hemisphere (solid). Then, as the peak solar insolation moves northward, the precipitation in the Southern Hemisphere decreases, whereas the precipitation in the Northern Hemisphere increases. At some point, the amount of precipitation in the Northern Hemisphere surpasses that of the Southern Hemisphere, and the position of the ITCZ jumps northward. The same process then occurs in reverse when moving from Northern Hemisphere summer to winter. This leads to a discontinuity in ITCZ position, despite precipitation at each location being continuous (Figs. 9a,b). In other words, because there are two precipitation maxima separated by a cool region, the ITCZ jumps between them, in contrast to the slab ocean simulation when one maximum moves back and forth. The "see saw" pattern of ITCZ seasonality has been discussed in the context of ITCZ modality (Adam 2023) and is not replicated without

TABLE 2. Key quantities diagnosed from our dynamic ocean simulations. Quantities are calculated as described in the text and averaged over the tropics, except ψ_O, which is averaged over the top 200 m of the ocean from 15° to 40°N to smooth out numerical noise, and α is taken to be the same value as in the slab ocean simulations.

	Atmosphere					Ocean							Coupled prediction			Coupled fit		
Simulation index	GMS_A (kJ kg^{-1})	ψ_A (10^9 kg s^{-1})	$\kappa_A C_A$ (10^{13} W K^{-1})	C_A (10^6 J m^{-2} K)	κ_A (10^6 m^2 s^{-1})	λ_A	GMS_O (kJ kg^{-1})	ψ_O (10^9 kg s^{-1})	u_{atm} (m s^{-1})	Δy	$\kappa_O C_O$ (10^{13} W K^{-1})	κ_O (10^3 m^2 s^{-1})	λ_O	$\kappa_C C_C$ (10^{13} W K^{-1})	κ_C (10^3 m^2 s^{-1})	λ_C	$\kappa_C C_C$ (10^{13} W K^{-1})	κ_C (10^3 m^2 s^{-1})	λ_C
1	7.4	65.1	2.3	8.8	2.6	0.59	60.1	13.7	−0.7	0.38	2.4	6.0	0.61	4.0	9.0	0.78	3.4	8.5	0.72
2	12.0	62.9	3.7	12.2	3.1	0.76	64.5	21.0	−1.2	0.44	3.2	8.0	0.70	6.8	17.0	1.02	4.9	12.1	0.86
3	15.7	54.0	4.9	15.7	3.1	0.86	62.9	20.9	−1.3	0.48	3.5	8.8	0.73	8.5	21.2	1.14	5.9	14.7	0.95
4	16.3	59.5	5.0	20.2	2.5	0.88	62.2	19.7	−1.3	0.49	3.7	9.4	0.76	8.8	21.9	1.16	6.8	16.9	1.02
5	16.5	56.0	5.1	27.9	1.8	0.88	63.6	23.6	−1.6	0.49	4.6	11.6	0.84	9.7	24.2	1.22	8.7	21.6	1.15
6	17.6	55.6	5.5	35.2	1.6	0.91	66.5	27.5	−1.9	0.49	5.4	13.4	0.90	10.9	27.1	1.29	10.6	26.4	1.27
7	19.4	53.1	6.0	41.9	1.4	0.96	69.8	31.4	−2.2	0.53	6.5	16.3	1.00	12.9	32.1	1.41	12.6	31.1	1.38

ocean dynamics even if the slab ocean is extremely deep (not shown but verified in simulations with a 500-m slab ocean). It is important to note that if the position of the ITCZ were calculated as the centroid of precipitation rather than the maximum, its seasonal cycle would be closer to sinusoidal.

Interestingly, summer precipitation increases significantly with warming (blue vs red line), while winter precipitation does not change as much. This may be due in part to the exponential relationship between temperature and humidity, in which a change in temperature has a larger effect on precipitation in a warmer (e.g., summer) climate.

The seasonal cycle of the ITCZ is shown for each dynamic ocean simulation in Fig. 9d. In all seven, the position of the ITCZ changes abruptly in spring and fall and remains roughly constant during the solstitial seasons. Note that the ITCZ is calculated as the average position of maximum precipitation over many years, so the smoothness of the transition is controlled by the interannual variability of the timing of the jump; in each year, the transition is discontinuous. It is also important to note that this sudden movement of the ITCZ between the hemispheres in the dynamic ocean case is different from that of a shallow slab ocean (Bordoni and Schneider 2008). In that case, there is a single ITCZ which is able to move far from the equator (much further than in the dynamic ocean case) because of the small heat capacity of the system. In the dynamic ocean case, there are almost always two ITCZs (Figs. 9a,b), and which ITCZ is stronger changes abruptly as a result of smooth changes in each. This result is a potential alternative hypothesis for the sudden monsoon onsets observed in several sectors.

The seasonal cycle of the ITCZ position decreases in amplitude somewhat with warming, but this is a much smaller effect than it was in the slab ocean simulation. The mechanism for the shrinking of the seasonal cycle with respect to warming is shown in Fig. 9e. Unlike in the slab ocean case, there is no annual mean SST maximum on the equator; instead, there are two off-equatorial maxima. The position of these maxima (despite being annual mean quantities) predicts the seasonal extrema of the ITCZ position very well (correlation 0.84). In other words, the latitude of the ITCZ during Northern Hemisphere summer is controlled by the latitude of the annual mean Northern Hemisphere SST maximum. As the SST minimum on the equator shrinks with warming, the SST maximum and the northernmost ITCZ position will move closer to the equator.

In summary, the ITCZ, its seasonal cycle, and its response to warming in the presence of a dynamic ocean are very different from those of a slab ocean aquaplanet. In the dynamic ocean simulation, there is a double ITCZ, with the summer hemisphere precipitation being much stronger, and abrupt seasonal transitions between the hemispheres. Additionally, the seasonal cycle amplitude decreases with warming, and this change is driven by shrinking of the SST minimum at the equator.

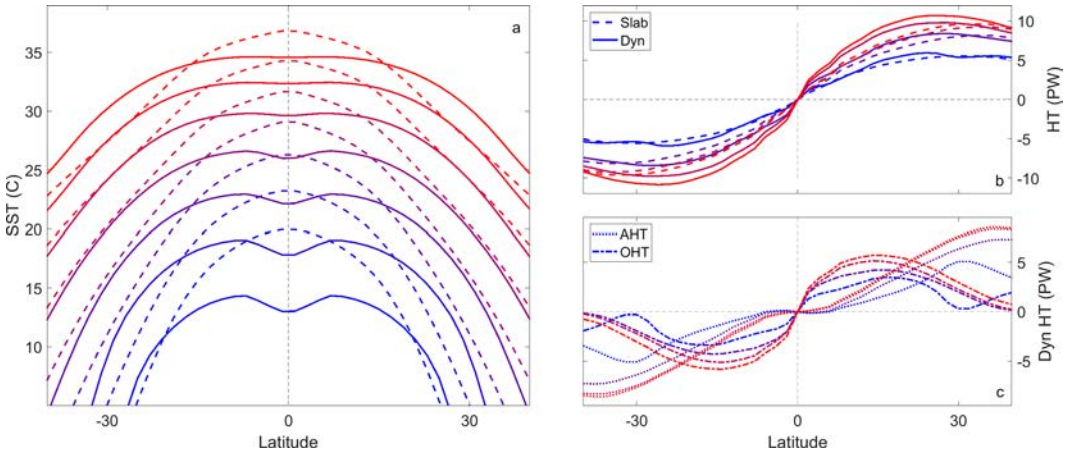

FIG. 8. (a) The simulated SST and (b),(c) heat transports in the slab ocean (dashed) and dynamic ocean (solid) simulations. (b) The total coupled heat transport, while (c) the atmospheric and OHT from the dynamic ocean simulations. (a) All seven simulations, while (b) and (c) plot only odd-numbered simulations for ease of viewing.

c. *Ridge simulation*

So far we have studied simulations without continents or barriers to ocean flow. However, it is important to consider the possible effects of boundaries that support ocean gyres. Do the main conclusions of our study also pertain to this more realistic case? To answer this question, we study a set of simulations with an infinitely thin barrier to ocean flow, i.e., "ridge simulations" (Ferreira et al. 2010; Wu et al. 2021) and apply our energy balance framework to them. The solutions are described in more detail in appendix C. These ridge simulations have ocean and atmosphere components that are identical to the dynamic ocean simulations already presented, except that there is a barrier running from the north pole and 35°S which blocks zonal ocean flow (top of Fig. 10). This single barrier is enough to cause significant zonal asymmetries; the simulations have a cold tongue and double ITCZ just west of the barrier, while they have warmer SSTs and stronger SSTs just east of it. Rather than studying these zonal asymmetries,

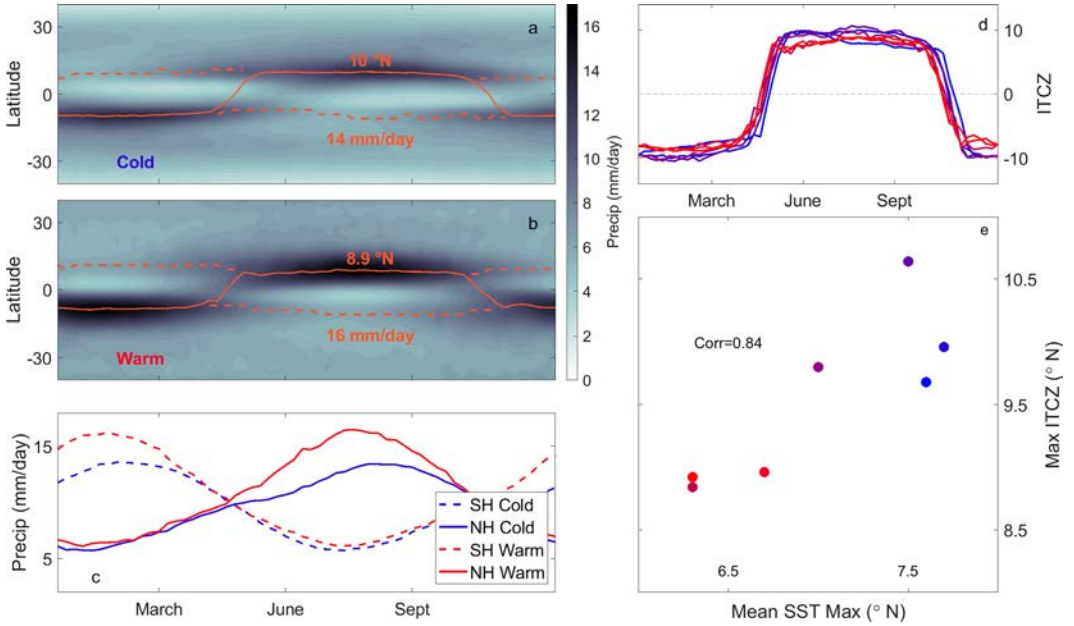

FIG. 9. The seasonal cycle of the ITCZ in the dynamic ocean. (a),(b) The zonal mean precipitation as a function of month and latitude in the (a) second coldest and (b) second warmest simulations. (c) The precipitation at 9°N and 9°S in the same two simulations. (d) The ITCZ position in each simulation over the seasonal cycle; (e) the relationship between the position of the annual mean SST maximum in the Northern Hemisphere and the maximum position of the ITCZ.

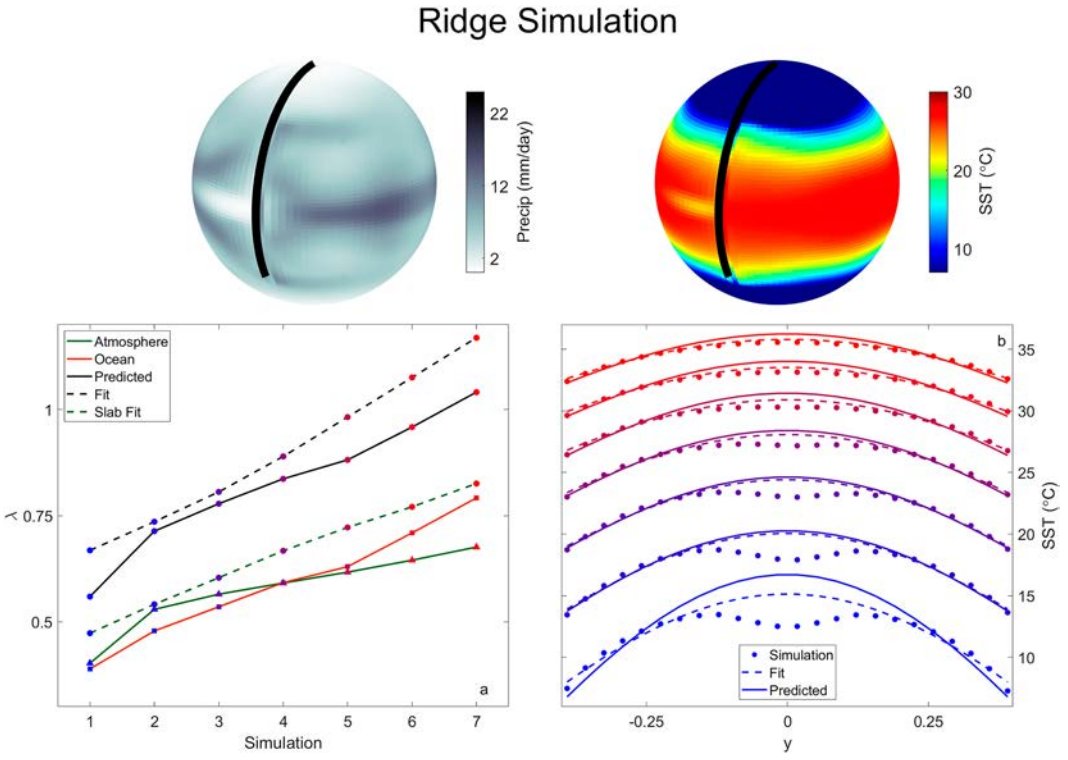

FIG. 10. The ridge simulations used in this study. The top half shows the continental configuration (the black line represents the ocean barrier), while the color represents (left) precipitation or (right) SST. The bottom half is as in Fig. 7, but for simulations with a single barrier to ocean flow stretching from the pole to 30°S.

we focus solely on applying our analytic model to them. Figure 10 shows the atmosphere, ocean, and coupled length scales (Fig. 10a), as well as the simulated and predicted SSTs (Fig. 10b).

In the ridge simulations, the atmosphere and ocean length scales are comparable and both increase with warming. Just as in the dynamic ocean simulations without a ridge, this leads to a large increase in the predicted coupled length scale, matching the simulated increase in length scale. These length scale changes lead to flatter SSTs, in broad agreement with the simulations (Fig. 10b). Other relevant quantities for the ridge simulations are shown and discussed in appendix C.

Flattening of SST gradients with warming has also been observed in paleoclimate studies, including in the presence of continents, indicating that our results are likely robust to ocean barriers and the presence of continents (e.g., Barron 1987; Judd et al. 2024).

4. Conclusions

In this work, we have studied the Hadley circulation, tropical SST gradients, the seasonal cycle of the ITCZ, and their responses to warming with and without a dynamic ocean. We find that in simulations with no ocean heat transport, there is a precipitation peak in the deep tropics which moves smoothly north and south with solar insolation over the course of the year. In warmer simulations, the equatorial SST peak flattens, weakening the Hadley cells, but an increase in gross moist stability means that the atmosphere transports more energy away from the equator. Additionally, as the climate warms, the ITCZ remains closer to the equator over the seasonal cycle due to the increasing heat capacity of the system.

In simulations with a dynamic ocean but no barriers to ocean flow, the trade winds lead to equatorial upwelling and an SST minimum at the equator. This means that precipitation has two off-equatorial peaks and is stronger in the summer hemisphere. Additionally, the dynamic ocean is very efficient at carrying energy away from the equator, making the SST gradient much flatter overall than in the absence of ocean dynamics. In response to warming, the SST gradient is smoothed even further, i.e., the extratropics and equatorial minimum both increase in temperature faster than the global mean due to strengthening heat transport in the atmosphere and ocean. The flat tropical SSTs lead to sudden ITCZ transitions between its summer and winter states, leading to a discontinuous seasonal cycle of ITCZ position.

Although this study has focused on simplified models, it has implications for the study of tropical climate on Earth. Perhaps most importantly, this work demonstrates that simple analytic frameworks can be useful to understand how circulations will change with warming. For example, we showed here that the Hadley circulation weakens as the climate warms; our analytic framework makes progress toward understanding this previously observed phenomenon (Held and Soden 2006; Vecchi and Soden 2007). Similarly, the tendency of SST gradients to flatten in warmer climates, i.e., polar amplification

(Judd et al. 2024), has been discussed at length, and the framework developed here helps to interpret this prediction and analyze how the structure of tropical SST depends on relevant quantities through our expression for λ. A similar framework could perhaps be applied to the Walker circulation, by replacing meridional gradients with zonal gradients and adding a simple representation of zonal ocean currents.

Furthermore, the contrast between our slab and dynamic ocean simulations shows that ocean heat transport is essential for the structure and seasonality of the ITCZ; a slab ocean will not capture even the basics of ITCZ seasonality (Zhao and Fedorov 2020; Tuckman et al. 2024, 2025). Specifically, we have shown that the normal state of the ITCZ over a dynamic ocean has two off-equatorial peaks, rather than a single peak on the equator. This may have implications for the "double ITCZ bias" in CMIP models (Popp and Lutsko 2017; Adam et al. 2018; Tian and Dong 2020; Popp et al. 2020; Kim et al. 2021): Many models exhibit a peak in precipitation just south of the equator, in addition to the observed peak a few degrees north of the equator (Schneider et al. 2014). Our work implies that this difference may be a manifestation of a precipitation peak south of the equator that is too strong rather than an unrealistic tendency to have a double ITCZ. The impact of the ocean on ITCZ seasonality also has significant implications. Abrupt precipitation transitions are societally important and may be caused or amplified by ocean dynamics smoothing SSTs. For example, it has been previously hypothesized that monsoon onset is a transition between Hadley cell regimes (Bordoni and Schneider 2008), our results suggest that they may simply be due to ocean dynamics flattening surface temperatures near the monsoon region.

Future research could illuminate these issues by adding more realistic features to our simulations. A natural way to do so would be to introduce hemispheric asymmetry through a prescribed asymmetric albedo or ocean heat transport and see how the ITCZ and its seasonal cycle change. Similarly, absorption and reflection of shortwave radiation by the atmosphere (and particularly clouds) have been shown to play a role in tropical dynamics (Donohoe et al. 2014a,b), including this effect would make the simulations more realistic. Last, an idealized continent might be added to our model, allowing exploration of how the seasonal cycle of the ITCZ is changed by the presence of land (Tuckman et al. 2024). The analytic framework introduced here may also be expanded to include such complications, helping to build intuition and understanding for how tropical circulations, temperatures, and precipitation depend on relevant parameters and change with warming.

Acknowledgments. P. J. Tuckman and J. Marshall acknowledge support from NSF Grant OCE-2023520 and the NASA MIT-GISS collaborative agreement. The authors thank two anonymous reviewers and Ori Adam for helpful comments.

Data availability statement. For the code and data from the simulations used in this study, please contact the corresponding author. A similar MITgcm configuration to the ones used in this study is available at https://github.com/MITgcm/verification_other/tree/master/cpl_gray%2Bswamp%2Bocn and discussed in Tuckman et al. (2025), although in that case there is a continent.

APPENDIX A

Theories of Hadley Cell Strength

To make our energy budget model analytically tractable, we assumed that the strength of the Hadley circulation is proportional to the local SST gradient. In this appendix, we review two well-known theories for Hadley cell strength and compare the predictions of these theories to the simulations studied. We find that the well-known Held–Hou theory of tropical circulations (Held and Hou 1980) does not match our simulations well, while a theory based on eddy momentum flux convergence does. This implies that Hadley cell strength is influenced by eddies carrying zonal momentum out of the tropics and, therefore, depends on several extratropical free troposphere quantities such as the lapse rate, tropopause height, and temperature variance (discussed below). Our simple assumption that the Hadley cell strength is linearly related to the tropical temperature gradient is used because it allows for an analytic solution of the system studied and is consistent with our simulations (Fig. 3a).

We begin with the framework set forth in Held and Hou (1980). This theory assumes that angular momentum is conserved within the Hadley cell, so if the zonal wind above the equator is zero, then angular momentum conservation will strengthen zonal winds off the equator. This can then be used to predict the potential temperature as a function of latitude and height, as well as a scaling for the vertical velocity at the equator. Held and Hou (1980) find that the normalized difference between the vertically averaged potential temperature at latitude y and the equator is

$$\frac{\theta(0) - \theta(y)}{\theta_0} = \frac{\omega^2 a^2}{gH}\frac{y^4}{2(1-y^2)}, \tag{A1}$$

where $\theta(y)$ is the potential temperature as a function of latitude, θ_0 is the latitudinally averaged potential temperature, ω and a are the angular rotation rate and radius of the Earth, g is the gravitational constant, and H is the tropopause height (m). Most of these parameters are constant, so the temperature gradient scales with the reciprocal of the tropopause height.

Held and Hou (1980) also predict that the vertical velocity at the equator scales as

$$w_{\mathrm{eq}} \sim g(H\Delta_H)^2/(\omega^2 a^2 \tau \Delta_v), \tag{A2}$$

where Δ_H and Δ_v are the normalized horizontal and vertical temperature gradients in radiative equilibrium (discussed below) and τ is the radiative time scale.

We diagnose Δ_H as follows. If we assume that OLR and NSR are in balance (i.e., the system is in radiative equilibrium, so $\theta \equiv \theta_e$), and use our expression for OLR from the

TABLE A1. Key parameters of the Held and Hou model. The Δ_H is the normalized horizontal temperature gradient in radiative equilibrium, and τ is the radiative time scale, calculated as discussed in the text. The tropopause height H is calculated by converting from the tropopause pressure (discussed in section 3a) to a height by assuming hydrostatic balance at the mean tropical temperature below the tropopause.

Simulation number	H (km)	τ (days)	Δ_H
1	10.5	69	0.52
2	11.6	88	0.50
3	12.8	111	0.49
4	14.0	139	0.48
5	15.4	177	0.47
6	17.1	230	0.46
7	19.1	281	0.45

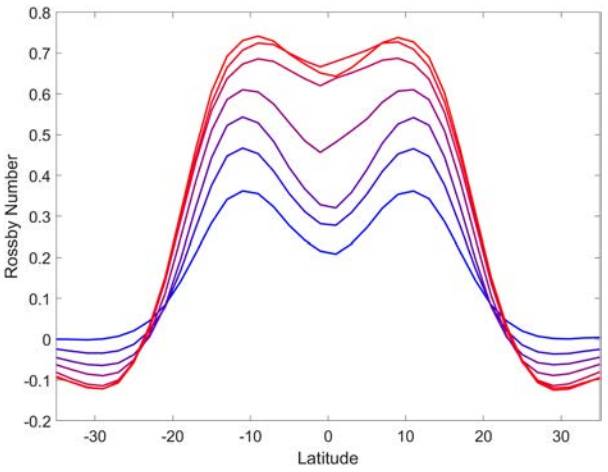

FIG. A1. Rossby number as a function of latitude at around 160 hPa. Blue represents cold simulations, and red represents warmer simulations.

main text, then $\theta_e(y) = [\mathrm{NSR}(y) - A_{\mathrm{out}}]/B_{\mathrm{out}}$. Held and Hou (1980) define Δ_H such that $\theta_e(y)/\theta_0 = 1 - \Delta_H(y^2 - 1/3)$; we evaluate this expression at the equator and 70°N to calculate a value of Δ_H. The radiative time scale τ can also be diagnosed from the simulations as C_A/B_{out}; B_{out} is the temperature dependence of the energy each column of air will lose in a second, and C_A converts this to a time scale. As discussed in the main text, A_{out} and B_{out} are diagnosed from the dependence of OLR on SST (Fig. 3) and C_A from the ratio of the MSE of a column to SST.

The final relevant quantity, Δ_v (defined as the radiative equilibrium difference in temperature between the surface and tropopause at the equator divided by the global mean temperature) is more difficult to diagnose and is therefore taken to be 1/8 as in Held and Hou (1980). Once we have calculated a predicted vertical velocity, this can be converted to a streamfunction by integrating from the equator to the approximate position of the streamfunction maximum (taken to be 10° latitude). The relevant parameters are shown in Table A1. These results will be compared with our simulations, but first, we review the predictions from a second theory. It is important to note that while the arguments in Held and Hou (1980) are for a dry atmosphere, they can be adapted to a moist system (Emanuel 1995) without significantly changing the relevant quantities.

The framework discussed above assumes that eddy-momentum fluxes do not play a role in the zonal-momentum balance of the deep tropics. However, synoptic eddies can influence the Hadley circulation by exchanging angular momentum with the tropics. This has led to a theory for Hadley cell strength that relates eddy momentum flux convergence in the tropics to the mean available potential energy in the baroclinic zone (Walker and Schneider 2006; Schneider and Bordoni 2008; Schneider and Walker 2008; O'Gorman and Schneider 2008; Levine and Schneider 2011). The Hadley streamfunction (ψ_A) is separated into an eddy momentum flux component (ψ_E) and a mean momentum flux component such that $\psi_E = \psi_A(1 - \mathrm{Ro})$, where Ro is the Rossby number calculated here as the negative ratio of relative vorticity to the Coriolis parameter. Figure A1 shows that the Rossby number increases with warming but is significantly less than one throughout the tropics in all simulations, indicating that eddies are important in setting the mean flow.

We now assume that ψ_E scales with the convergence of the eddy-momentum flux, and that the energy for the relevant eddies comes from the mean available potential energy (MAPE) of the baroclinic zone (Schneider and Walker 2008). Following Lorenz (1955), we calculate MAPE as

$$\mathrm{MAPE} = \frac{c_p p_s}{2g}\int_{p_s}^{p_t}\frac{dp}{p_s - p_t}\Gamma\left(\frac{p}{p_0}\right)^{\kappa}(\overline{\theta^2} - \overline{\theta}^2), \tag{A3}$$

where $\kappa = R/c_p \approx 2/7$, p_s is the surface pressure, the bar represents the average in the troposphere over 15°–45° in both hemispheres, p_t is the tropopause pressure, and Γ is proportional to the inverse lapse rate ($\Gamma = -\kappa\Delta p/\overline{p}\Delta\theta$, $\overline{p}$ is the average pressure in the troposphere and Δ represents the difference between tropopause and the surface). Due to the difficulty in using a discrete grid, MAPE is calculated between 985 and 350 hPa only, but our results are insensitive to this assumption. The relevant values are shown in Table A2.

MAPE is an important quantity because the available potential energy can be converted into eddy kinetic energy (EKE), which can then be related to eddy-momentum convergence via an eddy-length scale. If we assume that the rate at which MAPE converts to EKE does not change with warming, then ψ_E is proportional to MAPE multiplied by the width of the troposphere (Levine and Schneider 2011). Using the Rossby number discussed above, we can now predict ψ_A as

$$\psi_A \sim \frac{(p_s - p_t)\mathrm{MAPE}}{1 - \mathrm{Ro}}. \tag{A4}$$

This prediction and that of the Held and Hou model are compared to our simulations in Fig. A2.

TABLE A2. Key parameters of a model that assumes the Hadley cell strength is set by eddy momentum fluxes. The Γ is proportional to the inverse dry lapse rate ($\Gamma = -\kappa\Delta p/\overline{p}\Delta\theta$, $\overline{p}$ is the average pressure in the troposphere and Δp and $\Delta\theta$ represent the difference between the tropopause and the surface for pressure and potential temperature, respectively). The height of the troposphere is calculated as the tropopause pressure subtracted from 1000 hPa.

Simulation number	Γ [10^{-3} (1 K)$^{-1}$]	Δp (hPa)	MAPE (MJ m^{-2})
1	9.3	744	3.9
2	9.8	777	3.1
3	7.0	805	2.3
4	6.1	827	1.7
5	5.3	852	1.3
6	4.6	877	1.0
7	4.0	901	0.8

Overall, the simulations agree well with the scalings of the eddy convergence theory, but not with those of Held and Hou. This is consistent with the Rossby numbers being less than 1, as is clear from the simulations. The eddy convergence theory does not explicitly predict a relationship between the tropical SST gradient and the Hadley circulation, as it instead relies on extratropical free-tropospheric quantities; Fig. A2 simply displays how the predicted Hadley cell strength from that theory and the tropical temperature gradient are related in the simulations studied.

In summary, the analytic model developed in the main text assumed that the Hadley cell streamfunction is linearly related to a tropical temperature gradient. Previous literature indicates that Hadley circulation strength is more likely to be controlled by the energy available for extratropical eddies, which flux zonal momentum into the deep tropics. Although the theory developed in that literature does not include a prediction for the relationship between tropical temperature gradients and Hadley cell strength, its results are consistent with these quantities being linearly related across the simulations studied in this work.

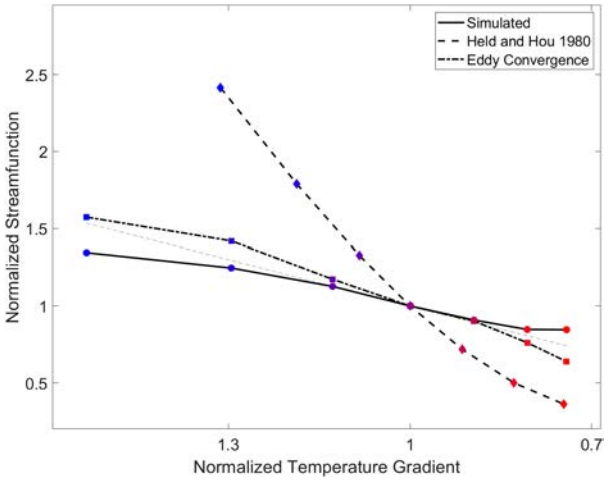

FIG. A2. Normalized predicted streamfunction as a function of normalized temperature gradients for constant α (dashed gray line), the simulations (circles, solid line), the Held and Hou theory (filled diamonds, dashed line), and the eddy convergence theory (filled squares, dash–dotted line).

APPENDIX B

Allowing GMS to Vary with Latitude

In the main text, we assumed that GMS was constant with latitude, so d/dy AHT was simply equal to GMS $d/dy\ \psi_A$ [based on Eq. (1c)]. However, since the surface MSE depends on the surface temperature, the difference between the tropopause and the surface MSE may depend on latitude. In this appendix, we examine how this can be added to the energy budget model and solve the resulting expression numerically in the slab and dynamic ocean cases.

We begin with our equation for the energy balance in the slab case [Eq. (1d)], but this time we write it in a way that allows for changes in GMS with latitude:

$$\frac{d}{dy}(\mathrm{GMS}\psi_A) + B_{\mathrm{out}}\mathrm{SST} + A_{\mathrm{out}} = \mathrm{NSR}. \tag{B1}$$

Now, substituting our expression for ψ_A and using the product rule:

$$-\alpha\frac{d}{dy}\mathrm{GMS}\frac{d}{dy}\mathrm{SST} - \alpha\mathrm{GMS}\frac{d^2}{dy^2}\mathrm{SST} + B_{\mathrm{out}}\mathrm{SST} = \mathrm{NSR} - A_{\mathrm{out}}. \tag{B2}$$

This equation is similar to Eq. (2), with the addition of a term that is proportional to d/dy GMS. As discussed in the main text, GMS is the difference between tropopause and surface MSE, and we will assume that the tropopause MSE is constant with latitude, as the free troposphere is efficient at spreading energy gradients (Held 2001). This means that

$$\frac{d}{dy}\mathrm{GMS} = -\frac{d}{dy}\mathrm{MSE}_{\mathrm{surface}}, \tag{B3}$$

and the tropopause MSE does not appear. We will now assume that the surface MSE is proportional to the surface temperature via an energy to temperature ratio of c_A which changes with warming. Note that this is not the same as the specific heat of air, as it is the change in energy of a parcel of air when the SST below it changes by 1°, not when its temperature changes by 1°. Our full energy budget equation becomes

$$\alpha c_A\left(\frac{d}{dy}\mathrm{SST}\right)^2 - \alpha\mathrm{GMS}\frac{d^2}{dy^2}\mathrm{SST} + B_{\mathrm{out}}\mathrm{SST} = \mathrm{NSR} - A_{\mathrm{out}}, \tag{B4}$$

where GMS still depends on latitude where it appears in the second term. To allow for a numerical solution, we use a

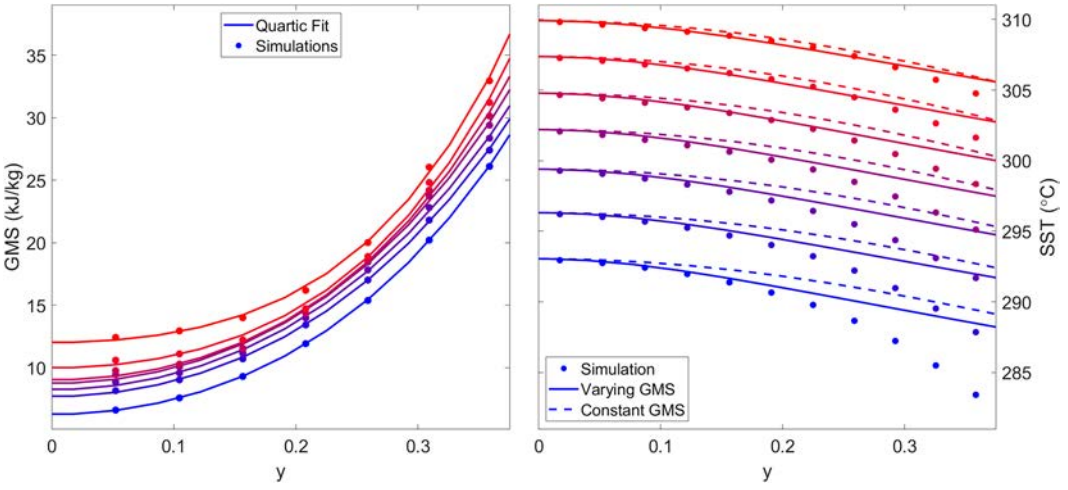

FIG. B1. (left) Simulated GMS and the calculated quartic fit as a function of latitude, and (right) the resulting numerical solutions with variable or constant GMS, all for the slab ocean simulations. As in previous figures, blue represents the cold simulations, and red represents the warmer simulations.

Taylor expansion about the equator assuming that GMS is quartic in y.

Figure B1 shows that this approximation is reasonable; the quartic fit (which depends on warming) matches reasonably well with the simulated values (left panel). Using a linear fit to calculate c_A, and the remaining constants set as before, we can numerically solve our energy budget equation starting at the equator, where d/dy SST = 0. The result is shown in the right panel of Fig. B1 and is compared to the solution that assumed a constant GMS. Varying GMS is generally a cooling effect, as it implies a higher GMS, and therefore diffusivity, in the cooler regions (away from the equator). This generally leads to improved fits in the cold simulations, where the previous version of the model overestimated surface temperatures. Both versions of the model do not do well outside of the deep tropics, as several of the assumptions made begin to break down.

We can apply the same procedure to the dynamic ocean simulations, though it does not change the result significantly. Intuitively, the SSTs are flatter in the dynamic ocean case, so the GMS will not change as quickly, especially since our simple model does not include the SST minimum on the equator.

The numerical results are shown in Fig. B2. The quartic fit for GMS is only conducted outside of the region of the SST minimum, so the resulting GMS values are very flat in the deep tropics. This flat GMS means that the d/dy GMS term is small, so the predicted SST is very similar to that of the constant GMS model (right panel).

In summary, a GMS that varies with latitude can be incorporated into our energy budget model, but the resulting expression must be solved numerically. Including this effect slightly improves the prediction in the slab ocean case, but

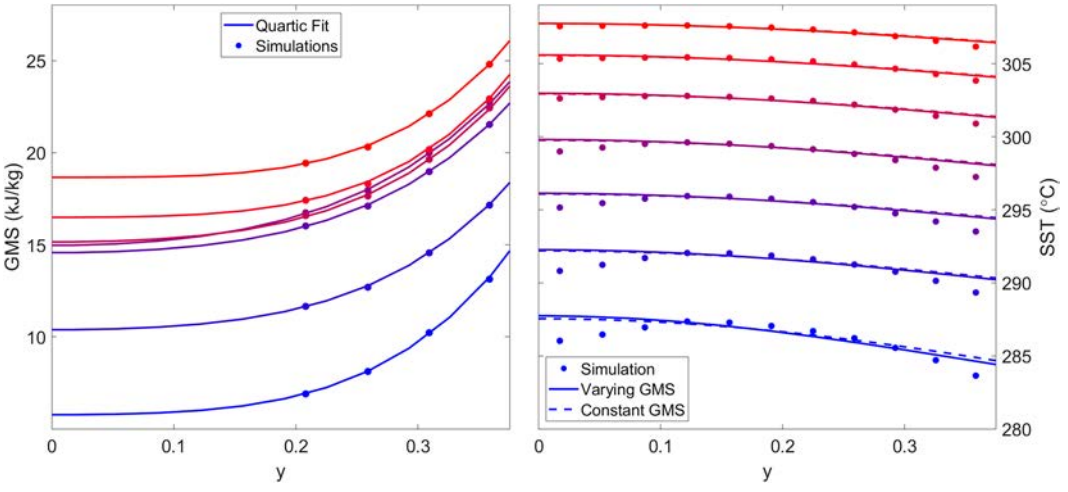

FIG. B2. As in Fig. B1, but for the dynamic ocean simulations.

does not make a significant difference in the dynamic ocean case because SST, and therefore GMS, is flat in the deep tropics.

APPENDIX C

The Ridge Simulations

In this appendix, we present further details of the simulations with a ridge discussed in section 3c. Figure C1 shows the same quantities as Fig. 6 but for the ridge simulations. Almost all features of the ridge simulations change with warming in the same way as did the dynamic ocean simulations: There are increases in precipitation (Fig. 6a), near-surface zonal wind (Fig. 6g), and atmospheric heat transport (Fig. 6i), and there is a slight flattening of SSTs (Fig. 6b). The Hadley cells represented through the streamfunctions (Figs. 6c,d) and the associated vertical velocity at 500 hPa (Fig. 6e) are strongest in the coldest simulation but thereafter do not change significantly with warming because the SST gradient starts so flat that it does not change significantly. As discussed in reference to dynamic ocean simulations, humidity (Fig. 6f), zonal wind (Fig. 6g), meridional current (Fig. 6h), and atmospheric heat transport (Fig. 6i) increase with warming. The ocean heat transport does not change significantly with warming despite the increase in mass transport (Fig. 6j), because the ocean stability decreases in the warmest climates (discussed below).

As shown in the main text, our analytic framework does reasonably well in predicting the flattening of the SST gradient in the ridge simulations. The relevant temperature-dependent parameters for the model are shown in Table C1, and the constant β is 8.5×10^9 kg m^{-1}. As expected, atmospheric GMS increases rather rapidly with warming, whereas mass transport (ψ_A) remains roughly constant. As in the previous results, this leads to an increase in $\kappa_A C_A$, in which κ_A

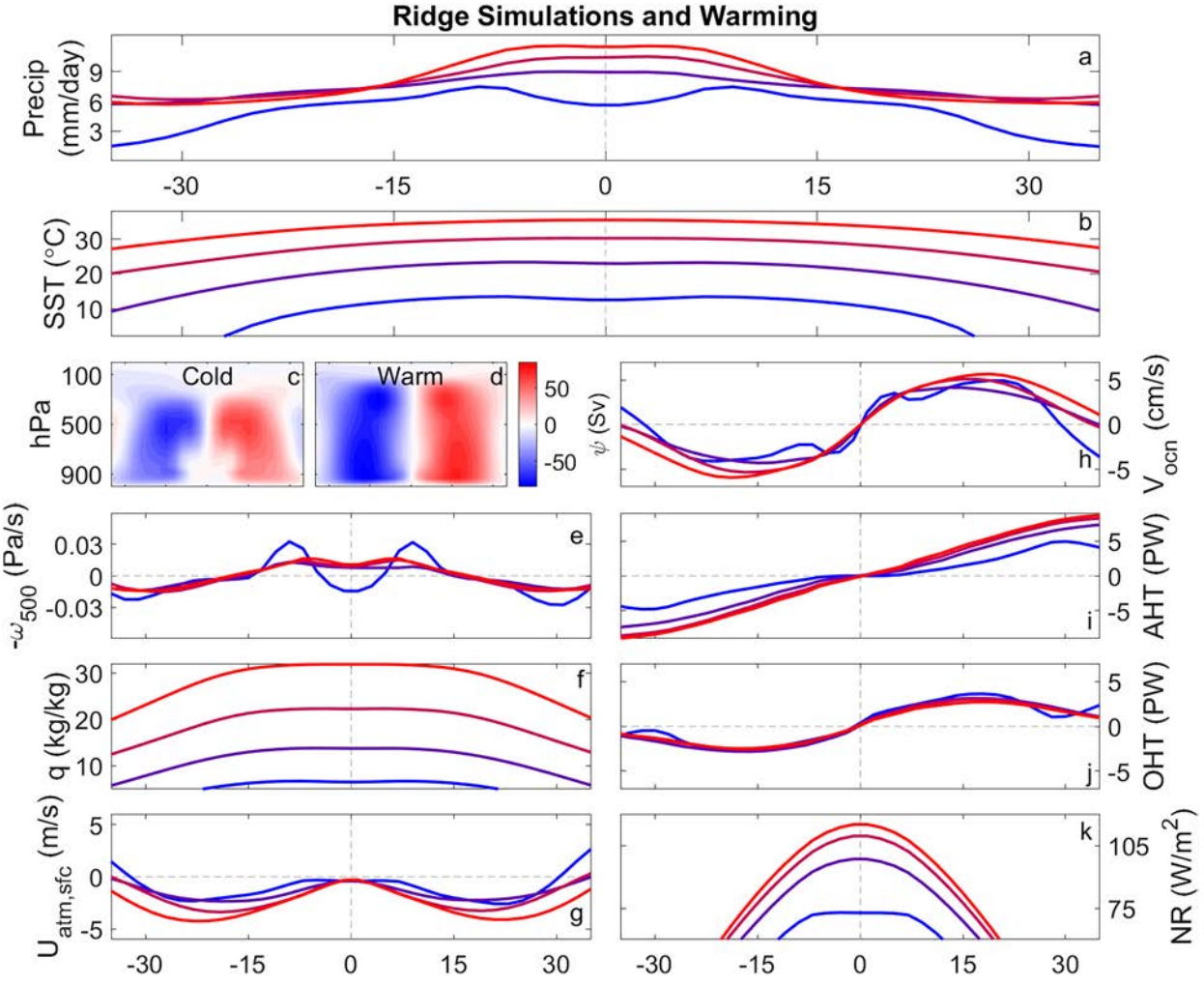

FIG. C1. As in Fig. 6, but for the ridge simulations, indices 1, 3, 5, and 7. The quantities shown are (a) precipitation, (b) SST, (c),(d) two sample Hadley cell streamfunctions, (e) vertical velocity at ~500 hPa, (f) near-surface specific humidity, (g) near-surface zonal wind, (h) near-surface meridional current, (i) atmospheric heat transport, (j) ocean heat transport, and (k) net radiation.

TABLE C1. Diagnostics from each of the seven ridge simulations. Quantities are calculated as described in the text and averaged over the tropics, except ψ_O, which is averaged over the top 200 m of the ocean from 15° to 40°N to smooth out numerical near-equatorial noise.

	Atmosphere						Ocean						Coupled prediction				Coupled fit			
Simulation index	GMS_A (kJ kg^{-1})	ψ_A (10^9 kg s^{-1})	$\kappa_A C_A$ (10^{13} W K^{-1})	C_A (10^6 J m^{-2} K^{-1})	κ_A (10^6 m^2 s^{-1})	λ_A	GMS_O (kJ kg^{-1})	ψ_O (10^9 kg s^{-1})	u_{atm} (m s^{-1})	Δy	$\kappa_O C_O$ (10^{13} W K^{-1})	κ_O (10^3 m^2 s^{-1})	λ_O	$\kappa_C C_C$ (10^{13} W K^{-1})	κ_C (10^3 m^2 s^{-1})	λ_C	$\kappa_C C_C$ (10^{13} W K^{-1})	κ_C (10^3 m^2 s^{-1})	λ_C
1	4.8	35.0	1.5	8.0	1.9	0.47	58.4	3.6	−1.2	0.30	1.2	3.0	0.43	2.7	6.7	0.64	2.9	7.3	0.67
2	8.3	33.0	2.6	11.1	2.3	0.63	66.9	13.1	−1.3	0.39	1.7	4.3	0.51	4.3	10.7	0.81	3.5	8.8	0.74
3	9.4	36.5	2.9	14.7	2.0	0.67	72.8	14.2	−1.5	0.40	2.0	5.1	0.56	5.0	12.4	0.87	4.3	10.6	0.81
4	10.3	37.8	3.2	19.8	1.6	0.70	65.6	15.4	−1.8	0.41	2.4	6.0	0.60	5.6	13.9	0.92	5.2	12.9	0.89
5	11.2	35.7	3.5	26.0	1.3	0.73	60.8	16.6	−2.0	0.39	2.6	6.5	0.63	6.1	15.1	0.96	6.3	15.7	0.98
6	12.3	38.1	3.8	33.5	1.1	0.76	55.8	20.2	−2.4	0.40	3.2	7.9	0.69	7.0	17.3	1.03	7.6	18.8	1.08
7	13.4	39.7	4.2	41.4	1.0	0.80	54.1	24.6	−2.7	0.42	3.8	9.6	0.76	8.0	19.9	1.11	0.9	22.2	1.17

decreases slightly and C_A increases rapidly. In other words, just as in the slab and dynamic ocean cases, the diffusivity of energy (κ_A) is slightly decreasing, but the energy contrast between the tropics and the extratropics is increasing (controlled by C_A), as is the atmospheric GMS. This leads to a more efficient smoothing of the SST gradient by the atmosphere (i.e., λ_A increasing) and stronger atmospheric heat transport.

The ocean in the ridge simulations behaves slightly differently than in the dynamic ocean simulations, but the main results are not altered. Specifically, while in the dynamic ocean simulations, GMS_O increased monotonically with warming, in the ridge simulations it peaks in the third simulation and decreases with warming thereafter. However, the increase in mass transport, driven by an increase in U_{atm}, more than compensates, leading to an increase in $\kappa_O C_O$ and therefore λ_O. Together, this leads to an increase in the coupled diffusivity and length scale, matching the fitted parameters.

In summary, while the presence of a ridge profoundly changes the zonal structure of the tropics (by, for example, inducing a Walker circulation and cold tongue, not shown), the broad meridional structure of the tropics is still well understood by our simplified analytic framework.

REFERENCES

Adam, O., 2021: Dynamic and energetic constraints on the modality and position of the intertropical convergence zone in an aquaplanet. *J. Climate*, **34**, 527–543, https://doi.org/10.1175/JCLI-D-20-0128.1.

——, 2023: The influence of equatorial cooling on axially symmetric atmospheric circulation forced by annually averaged heating. *J. Climate*, **36**, 7451–7464, https://doi.org/10.1175/JCLI-D-23-0157.1.

——, T. Bischoff, and T. Schneider, 2016: Seasonal and interannual variations of the energy flux equator and ITCZ. Part II: Zonally varying shifts of the ITCZ. *J. Climate*, **29**, 7281–7293, https://doi.org/10.1175/JCLI-D-15-0710.1.

——, T. Schneider, and F. Brient, 2018: Regional and seasonal variations of the double-ITCZ bias in CMIP5 models. *Climate Dyn.*, **51**, 101–117, https://doi.org/10.1007/s00382-017-3909-1.

——, A. Farnsworth, and D. J. Lunt, 2023: Modality of the tropical rain belt across models and simulated climates. *J. Climate*, **36**, 1331–1345, https://doi.org/10.1175/JCLI-D-22-0521.1.

Adcroft, A., J.-M. Campin, C. Hill, and J. Marshall, 2004: Implementation of an atmosphere–ocean general circulation model on the expanded spherical cube. *Mon. Wea. Rev.*, **132**, 2845–2863, https://doi.org/10.1175/MWR2823.1.

Afargan-Gerstman, H., and O. Adam, 2020: Nonlinear damping of ITCZ migrations due to Ekman ocean energy transport. *Geophys. Res. Lett.*, **47**, e2019GL086445, https://doi.org/10.1029/2019GL086445.

Ahmed, F., and J. D. Neelin, 2019: Explaining scales and statistics of tropical precipitation clusters with a stochastic model. *J. Atmos. Sci.*, **76**, 3063–3087, https://doi.org/10.1175/JAS-D-18-0368.1.

Barron, E. J., 1987: Eocene equator-to-pole surface ocean temperatures: A significant climate problem? *Paleoceanogr. Paleoclimatol.*, **2**, 729–739, https://doi.org/10.1029/PA002i006p00729.

Bischoff, T., and T. Schneider, 2016: The equatorial energy balance, ITCZ position, and double-ITCZ bifurcations. *J. Climate*, **29**, 2997–3013, https://doi.org/10.1175/JCLI-D-15-0328.1.

Blackburn, M., and B. J. Hoskins, 2013: Context and aims of the aqua-planet experiment. *J. Meteor. Soc. Japan*, **91A**, 1–15, https://doi.org/10.2151/jmsj.2013-A01.

——, and Coauthors, 2013: The Aqua-Planet Experiment (APE): CONTROL SST simulation. *J. Meteor. Soc. Japan*, **91A**, 17–56, https://doi.org/10.2151/jmsj.2013-A02.

Bordoni, S., and T. Schneider, 2008: Monsoons as eddy-mediated regime transitions of the tropical overturning circulation. *Nat. Geosci.*, **1**, 515–519, https://doi.org/10.1038/ngeo248.

Broccoli, A. J., K. A. Dahl, and R. J. Stouffer, 2006: Response of the ITCZ to Northern Hemisphere cooling. *Geophys. Res. Lett.*, **33**, L01702, https://doi.org/10.1029/2005GL024546.

Buckley, M. W., and J. Marshall, 2016: Observations, inferences, and mechanisms of the Atlantic meridional overturning circulation: A review. *Rev. Geophys.*, **54**, 5–63, https://doi.org/10.1002/2015RG000493.

Burls, N. J., and A. V. Fedorov, 2014: Simulating Pliocene warmth and a permanent El Niño-like state: The role of cloud albedo. *Paleoceanogr. Paleoclimatol.*, **29**, 893–910, https://doi.org/10.1002/2014PA002644.

——, and ——, 2017: Wetter subtropics in a warmer world: Contrasting past and future hydrological cycles. *Proc. Natl. Acad. Sci. USA*, **114**, 12 888–12 893, https://doi.org/10.1073/pnas.1703421114.

Byrne, M. P., and P. A. O'Gorman, 2013: Land–ocean warming contrast over a wide range of climates: Convective quasi-equilibrium theory and idealized simulations. *J. Climate*, **26**, 4000–4016, https://doi.org/10.1175/JCLI-D-12-00262.1.

——, A. G. Pendergrass, A. D. Rapp, and K. R. Wodzicki, 2018: Response of the intertropical convergence zone to climate change: Location, width, and strength. *Curr. Climate Change Rep.*, **4**, 355–370, https://doi.org/10.1007/s40641-018-0110-5.

Chemke, R., 2021: Future changes in the Hadley circulation: The role of ocean heat transport. *Geophys. Res. Lett.*, **48**, e2020GL091372, https://doi.org/10.1029/2020GL091372.

——, and L. M. Polvani, 2018: Ocean circulation reduces the Hadley cell response to increased greenhouse gases. *Geophys. Res. Lett.*, **45**, 9197–9205, https://doi.org/10.1029/2018GL079070.

——, and ——, 2021: Elucidating the mechanisms responsible for Hadley cell weakening under 4 × CO_2 forcing. *Geophys. Res. Lett.*, **48**, e2020GL090348, https://doi.org/10.1029/2020GL090348.

Chou, C., and J. D. Neelin, 2004: Mechanisms of global warming impacts on regional tropical precipitation. *J. Climate*, **17**, 2688–2701, https://doi.org/10.1175/1520-0442(2004)017<2688:MOGWIO>2.0.CO;2.

Clapeyron, P. E., 1834: Mémoire sur la puissance Motrice de la Chaleur. 39 pp., https://www3.nd.edu/~powers/ame.20231/clapeyron1834.pdf.

Clement, A. C., 2006: The role of the ocean in the seasonal cycle of the Hadley circulation. *J. Atmos. Sci.*, **63**, 3351–3365, https://doi.org/10.1175/JAS3811.1.

Codron, F., 2012: Ekman heat transport for slab oceans. *Climate Dyn.*, **38**, 379–389, https://doi.org/10.1007/s00382-011-1031-3.

Craig, G. C., and J. M. Mack, 2013: A coarsening model for self-organization of tropical convection. *J. Geophys. Res. Atmos.*, **118**, 8761–8769, https://doi.org/10.1002/jgrd.50674.

Cronin, T. W., and K. A. Emanuel, 2013: The climate time scale in the approach to radiative-convective equilibrium. *J. Adv. Model. Earth Syst.*, **5**, 843–849, https://doi.org/10.1002/jame.20049.

Czaja, A., and J. Marshall, 2006: The partitioning of poleward heat transport between the atmosphere and ocean. *J. Atmos. Sci.*, **63**, 1498–1511, https://doi.org/10.1175/JAS3695.1.

D'Agostino, R., P. Lionello, O. Adam, and T. Schneider, 2017: Factors controlling Hadley circulation changes from the last glacial maximum to the end of the 21st century. *Geophys. Res. Lett.*, **44**, 8585–8591, https://doi.org/10.1002/2017GL074533.

Donohoe, A., K. C. Armour, A. G. Pendergrass, and D. S. Battisti, 2014a: Shortwave and longwave radiative contributions to global warming under increasing CO_2. *Proc. Natl. Acad. Sci. USA*, **111**, 16 700–16 705, https://doi.org/10.1073/pnas.1412190111.

——, D. M. W. Frierson, and D. S. Battisti, 2014b: The effect of ocean mixed layer depth on climate in slab ocean aquaplanet experiments. *Climate Dyn.*, **43**, 1041–1055, https://doi.org/10.1007/s00382-013-1843-4.

Emanuel, K., 2019: Inferences from simple models of slow, convectively coupled processes. *J. Atmos. Sci.*, **76**, 195–208, https://doi.org/10.1175/JAS-D-18-0090.1.

Emanuel, K. A., 1995: On thermally direct circulations in moist atmospheres. *J. Atmos. Sci.*, **52**, 1529–1534, https://doi.org/10.1175/1520-0469(1995)052<1529:OTDCIM>2.0.CO;2.

——, J. David Neelin, and C. S. Bretherton, 1994: On large-scale circulations in convecting atmospheres. *Quart. J. Roy. Meteor. Soc.*, **120**, 1111–1143, https://doi.org/10.1002/qj.49712051902.

England, M. R., and N. Feldl, 2024: Robust polar amplification in ice-free climates relies on ocean heat transport and cloud radiative effects. *J. Climate*, **37**, 2179–2197, https://doi.org/10.1175/JCLI-D-23-0151.1.

Feldl, N., and S. Bordoni, 2016: Characterizing the Hadley circulation response through regional climate feedbacks. *J. Climate*, **29**, 613–622, https://doi.org/10.1175/JCLI-D-15-0424.1.

Ferreira, D., J. Marshall, and J.-M. Campin, 2010: Localization of deep water formation: Role of atmospheric moisture transport and geometrical constraints on ocean circulation. *J. Climate*, **23**, 1456–1476, https://doi.org/10.1175/2009JCLI3197.1.

Frierson, D. M. W., and Y.-T. Hwang, 2012: Extratropical influence on ITCZ shifts in slab ocean simulations of global warming. *J. Climate*, **25**, 720–733, https://doi.org/10.1175/JCLI-D-11-00116.1.

——, I. M. Held, and P. Zurita-Gotor, 2007: A gray-radiation aquaplanet moist GCM. Part II: Energy transports in altered climates. *J. Atmos. Sci.*, **64**, 1680–1693, https://doi.org/10.1175/JAS3913.1.

——, and Coauthors, 2013: Contribution of ocean overturning circulation to tropical rainfall peak in the Northern Hemisphere. *Nat. Geosci.*, **6**, 940–944, https://doi.org/10.1038/ngeo1987.

Gastineau, G., L. Li, and H. L. Treut, 2009: The Hadley and Walker circulation changes in global warming conditions described by idealized atmospheric simulations. *J. Climate*, **22**, 3993–4013, https://doi.org/10.1175/2009JCLI2794.1.

Geen, R., F. H. Lambert, and G. K. Vallis, 2019: Processes and timescales in onset and withdrawal of "aquaplanet monsoons". *J. Atmos. Sci.*, **76**, 2357–2373, https://doi.org/10.1175/JAS-D-18-0214.1.

Green, B., and J. Marshall, 2017: Coupling of trade winds with ocean circulation damps ITCZ shifts. *J. Climate*, **30**, 4395–4411, https://doi.org/10.1175/JCLI-D-16-0818.1.

——, ——, and J.-M. Campin, 2019: The 'sticky' ITCZ: Ocean-moderated ITCZ shifts. *Climate Dyn.*, **53**, 1–19, https://doi.org/10.1007/s00382-019-04623-5.

Held, I. M., 2001: The partitioning of the poleward energy transport between the tropical ocean and atmosphere. *J. Atmos. Sci.*, **58**, 943–948, https://doi.org/10.1175/1520-0469(2001)058<0943:TPOTPE>2.0.CO;2.

——, and A. Y. Hou, 1980: Nonlinear axially symmetric circulations in a nearly inviscid atmosphere. *J. Atmos. Sci.*, **37**, 515–533, https://doi.org/10.1175/1520-0469(1980)037<0515:NASCIA>2.0.CO;2.

——, and B. J. Soden, 2006: Robust responses of the hydrological cycle to global warming. *J. Climate*, **19**, 5686–5699, https://doi.org/10.1175/JCLI3990.1.

Hilgenbrink, C. C., and D. L. Hartmann, 2018: The response of Hadley circulation extent to an idealized representation of poleward ocean heat transport in an aquaplanet GCM. *J. Climate*, **31**, 9753–9770, https://doi.org/10.1175/JCLI-D-18-0324.1.

Hottovy, S., and S. N. Stechmann, 2015: A spatiotemporal stochastic model for tropical precipitation and water vapor dynamics. *J. Atmos. Sci.*, **72**, 4721–4738, https://doi.org/10.1175/JAS-D-15-0119.1.

Hu, Y., H. Huang, and C. Zhou, 2018: Widening and weakening of the Hadley circulation under global warming. *Sci. Bull.*, **63**, 640–644, https://doi.org/10.1016/j.scib.2018.04.020.

Huang, Y., Y. Xia, and X. Tan, 2017: On the pattern of CO_2 radiative forcing and poleward energy transport. *J. Geophys. Res. Atmos.*, **122**, 10 578–10 593, https://doi.org/10.1002/2017JD027221.

Hwang, Y.-T., and D. M. W. Frierson, 2010: Increasing atmospheric poleward energy transport with global warming. *Geophys. Res. Lett.*, **37**, L24807, https://doi.org/10.1029/2010GL045440.

Inoue, K., and L. E. Back, 2017: Gross moist stability analysis: Assessment of satellite-based products in the GMS plane. *J. Atmos. Sci.*, **74**, 1819–1837, https://doi.org/10.1175/JAS-D-16-0218.1.

Judd, E. J., J. E. Tierney, D. J. Lunt, I. P. Montañez, B. T. Huber, S. L. Wing, and P. J. Valdes, 2024: A 485-million-year history of Earth's surface temperature. *Science*, **385**, eadk3705, https://doi.org/10.1126/science.adk3705.

Kang, S. M., Y. Shin, and S.-P. Xie, 2018: Extratropical forcing and tropical rainfall distribution: Energetics framework and ocean Ekman advection. *npj Climate Atmos. Sci.*, **1**, 20172, https://doi.org/10.1038/s41612-017-0004-6.

Kim, H., S. M. Kang, K. Takahashi, A. Donohoe, and A. G. Pendergrass, 2021: Mechanisms of tropical precipitation biases in climate models. *Climate Dyn.*, **56**, 17–27, https://doi.org/10.1007/s00382-020-05325-z.

Koll, D. D. B., and T. W. Cronin, 2018: Earth's outgoing longwave radiation linear due to H_2O greenhouse effect. *Proc. Natl. Acad. Sci. USA*, **115**, 10 293–10 298, https://doi.org/10.1073/pnas.1809868115.

Levine, X. J., and T. Schneider, 2011: Response of the Hadley circulation to climate change in an aquaplanet GCM coupled to a simple representation of ocean heat transport. *J. Atmos. Sci.*, **68**, 769–783, https://doi.org/10.1175/2010JAS3553.1.

Lionello, P., R. D'Agostino, D. Ferreira, H. Nguyen, and M. S. Singh, 2024: The Hadley circulation in a changing climate. *Ann. N. Y. Acad. Sci.*, **1534**, 69–93, https://doi.org/10.1111/nyas.15114.

Lorenz, E. N., 1955: Available potential energy and the maintenance of the general circulation. *Tellus*, **7**, 157–167, https://doi.org/10.1111/j.2153-3490.1955.tb01148.x.

Ma, J., R. Chadwick, K.-H. Seo, C. Dong, G. Huang, G. R. Foltz, and J. H. Jiang, 2018: Responses of the tropical atmospheric circulation to climate change and connection to the hydrological cycle. *Annu. Rev. Earth Planet. Sci.*, **46**, 549–580, https://doi.org/10.1146/annurev-earth-082517-010102.

Marshall, J., A. Adcroft, C. Hill, L. Perelman, and C. Heisey, 1997: A finite-volume, incompressible Navier Stokes model for studies of the ocean on parallel computers. *J. Geophys. Res.*, **102**, 5753–5766, https://doi.org/10.1029/96JC02775.

——, A. Donohoe, D. Ferreira, and D. McGee, 2014: The ocean's role in setting the mean position of the Inter-Tropical Convergence Zone. *Climate Dyn.*, **42**, 1967–1979, https://doi.org/10.1007/s00382-013-1767-z.

Moreno-Chamarro, E., J. Marshall, and T. L. Delworth, 2020: Linking ITCZ migrations to the AMOC and North Atlantic/Pacific SST decadal variability. *J. Climate*, **33**, 893–905, https://doi.org/10.1175/JCLI-D-19-0258.1.

Neelin, J. D., and I. M. Held, 1987: Modeling tropical convergence based on the moist static energy budget. *Mon. Wea. Rev.*, **115**, 3–12, https://doi.org/10.1175/1520-0493(1987)115<0003:MTCBOT>2.0.CO;2.

O'Gorman, P. A., and T. Schneider, 2008: Energy of midlatitude transient eddies in idealized simulations of changed climates. *J. Climate*, **21**, 5797–5806, https://doi.org/10.1175/2008JCLI2099.1.

Popp, M., and N. J. Lutsko, 2017: Quantifying the zonal-mean structure of tropical precipitation. *Geophys. Res. Lett.*, **44**, 9470–9478, https://doi.org/10.1002/2017GL075235.

——, ——, and S. Bony, 2020: Weaker links between zonal convective clustering and ITCZ width in climate models than in observations. *Geophys. Res. Lett.*, **47**, e2020GL090479, https://doi.org/10.1029/2020GL090479.

Rantanen, M., A. Y. Karpechko, A. Lipponen, K. Nordling, O. Hyvärinen, K. Ruosteenoja, T. Vihma, and A. Laaksonen, 2022: The Arctic has warmed nearly four times faster than the globe since 1979. *Commun. Earth Environ.*, **3**, 168, https://doi.org/10.1038/s43247-022-00498-3.

Raymond, D. J., S. L. Sessions, A. H. Sobel, and Z. Fuchs, 2009: The mechanics of gross moist stability. *J. Adv. Model. Earth Syst.*, **1**, 9, https://doi.org/10.3894/JAMES.2009.1.9.

Rose, B. E. J., and J. Marshall, 2009: Ocean heat transport, sea ice, and multiple climate states: Insights from energy balance models. *J. Atmos. Sci.*, **66**, 2828–2843, https://doi.org/10.1175/2009JAS3039.1.

Santer, B. D., and Coauthors, 2003a: Behavior of tropopause height and atmospheric temperature in models, reanalyses, and observations: Decadal changes. *J. Geophys. Res.*, **108**, 4002, https://doi.org/10.1029/2002JD002258.

——, and Coauthors, 2003b: Contributions of anthropogenic and natural forcing to recent tropopause height changes. *Science*, **301**, 479–483, https://doi.org/10.1126/science.1084123.

Schneider, T., and C. C. Walker, 2008: Scaling laws and regime transitions of macroturbulence in dry atmospheres. *J. Atmos. Sci.*, **65**, 2153–2173, https://doi.org/10.1175/2007JAS2616.1.

——, and S. Bordoni, 2008: Eddy-mediated regime transitions in the seasonal cycle of a Hadley circulation and implications for monsoon dynamics. *J. Atmos. Sci.*, **65**, 915–934, https://doi.org/10.1175/2007JAS2415.1.

——, T. Bischoff, and G. H. Haug, 2014: Migrations and dynamics of the intertropical convergence zone. *Nature*, **513**, 45–53, https://doi.org/10.1038/nature13636.

Siler, N., G. H. Roe, and K. C. Armour, 2018: Insights into the zonal-mean response of the hydrologic cycle to global warming from a diffusive energy balance model. *J. Climate*, **31**, 7481–7493, https://doi.org/10.1175/JCLI-D-18-0081.1.

Sobel, A. H., and S. J. Camargo, 2011: Projected future seasonal changes in tropical summer climate. *J. Climate*, **24**, 473–487, https://doi.org/10.1175/2010JCLI3748.1.

Tian, B., and X. Dong, 2020: The double-ITCZ bias in CMIP3, CMIP5, and CMIP6 models based on annual mean precipitation. *Geophys. Res. Lett.*, **47**, e2020GL087232, https://doi.org/10.1029/2020GL087232.

Tuckman, P. J., 2025: Understanding ENSO weakening in warmer climates. *Geophys. Res. Lett.*, **52**, e2024GL113124, https://doi.org/10.1029/2024GL113124.

——, J. Smyth, N. J. Lutsko, and J. Marshall, 2024: The zonal seasonal cycle of tropical precipitation: Introducing the Indo-Pacific monsoonal mode. *J. Climate*, **37**, 3807–3824, https://doi.org/10.1175/JCLI-D-23-0125.1.

——, J. E. Smyth, J. Li, N. J. Lutsko, and J. Marshall, 2025: ENSO and West Pacific seasonality driven by the South Asian monsoon. *Geophys. Res. Lett.*, **52**, e2024GL111084, https://doi.org/10.1029/2024GL111084.

Vecchi, G. A., and B. J. Soden, 2007: Global warming and the weakening of the tropical circulation. *J. Climate*, **20**, 4316–4340, https://doi.org/10.1175/JCLI4258.1.

Walker, C. C., and T. Schneider, 2006: Eddy influences on Hadley circulations: Simulations with an idealized GCM. *J. Atmos. Sci.*, **63**, 3333–3350, https://doi.org/10.1175/JAS3821.1.

Wang, Z., E. K. Schneider, and N. J. Burls, 2019: The sensitivity of climatological SST to slab ocean model thickness. *Climate Dyn.*, **53**, 5709–5723, https://doi.org/10.1007/s00382-019-04892-0.

Wu, X., K. A. Reed, C. L. P. Wolfe, G. M. Marques, S. D. Bachman, and F. O. Bryan, 2021: Coupled aqua and ridge planets in the Community Earth System Model. *J. Adv. Model. Earth Syst.*, **13**, e2020MS002418, https://doi.org/10.1029/2020MS002418.

Yu, J.-Y., C. Chou, and J. D. Neelin, 1998: Estimating the gross moist stability of the tropical atmosphere. *J. Atmos. Sci.*, **55**, 1354–1372, https://doi.org/10.1175/1520-0469(1998)055<1354:ETGMSO>2.0.CO;2.

Zhang, R., and T. L. Delworth, 2005: Simulated tropical response to a substantial weakening of the Atlantic thermohaline circulation. *J. Climate*, **18**, 1853–1860, https://doi.org/10.1175/JCLI3460.1.

Zhao, B., and A. Fedorov, 2020: The seesaw response of the intertropical and South Pacific convergence zones to hemispherically asymmetric thermal forcing. *Climate Dyn.*, **54**, 1639–1653, https://doi.org/10.1007/s00382-019-05076-6.